

COSMIC RAYS AND NON-THERMAL EMISSION INDUCED BY ACCRETION OF COOL GAS ONTO THE GALACTIC DISK

SUSUMU INOUE¹, YASUNOBU UCHIYAMA², MASANORI ARAKAWA^{2,1}, MATTHIEU RENAUD³, AND KEIICHI WADA⁴

ApJ, submitted

ABSTRACT

On both observational and theoretical grounds, the disk of our Galaxy is believed to be accreting cool gas with temperature $\lesssim 10^5$ K via the halo at a rate of order $1 M_{\odot} \text{ yr}^{-1}$. High velocity clouds (HVCs), observed to be traveling in the halo at velocities of a few 100 km s^{-1} relative to the disk, are likely manifestations of this process, some of which can directly impact the disk at such velocities, especially in the outer regions of the Galaxy. We address the possibility of particle acceleration in shocks triggered by such HVC accretion events, and the detectability of consequent non-thermal emission from the radio to gamma-ray bands as well as high-energy neutrinos. For plausible values of shock velocity $\sim 300 \text{ km s}^{-1}$ and magnetic field strength $\sim 0.3 - 10 \mu\text{G}$, electrons and protons may be accelerated up to $\sim 1 - 10 \text{ TeV}$ and $\sim 30 - 10^3 \text{ TeV}$, respectively, in sufficiently strong adiabatic shocks during their lifetime of $\sim 10^6 \text{ yr}$. The resultant pion decay and inverse Compton gamma-rays may be the origin of some unidentified GeV-TeV sources in the Galactic Plane, particularly the “dark” source HESS J1503-582 that is spatially coincident with anomalous HI structure known as a “forbidden-velocity wing”. Correlation of their locations with star-forming regions may be weak, absent, or even opposite. Non-thermal radio and X-ray emission due to primary and/or secondary electrons may be detectable in some cases with deeper observations. The contribution of HVC accretion to Galactic cosmic rays is expected to be subdominant, $\lesssim 5\%$ in total, but could be non-negligible in the outer Galaxy. As the thermal emission induced by HVC accretion could be difficult to detect, observations of such phenomena may offer a unique perspective on probing gas accretion processes onto the Milky Way and other galaxies.

Subject headings: acceleration of particles — cosmic rays — Galaxy: disk — gamma rays: ISM — ISM: clouds — radiation mechanisms: non-thermal

1. INTRODUCTION

1.1. Gas accretion onto galaxies

Gas accretion onto galaxies over cosmological timescales is understood to be one of the key processes governing their formation and evolution, as deduced from a variety of observational and theoretical considerations (for reviews, see e.g. Sancisi et al. 2008; Putman et al. 2012; Sánchez Almeida et al. 2014; Fox & Davé 2017). To sustain the star formation rate of the Milky Way that is inferred to have been approximately constant over the last several Gyr, the Galactic disk must have been continuously supplied with gas at a rate of order $\dot{M}_{\text{acc,SF}} \sim 1 M_{\odot} \text{ yr}^{-1}$. Potential sources of the accreting gas include the intergalactic medium (IGM) channeled along filaments of the cosmic web, gas stripped from satellite galaxies, condensation out of hot halo gas via thermal instabilities, and gas recycled from supernova (SN)-driven fountains or winds from the disk (Oort 1970; Shapiro & Field 1976; Richter 2017). The observed metallicity distribution of long-lived disk stars indicates that such accreting gas must be relatively metal-poor (Larson 1972; Finlator 2017), favoring the IGM, satellite and/or halo gas as the dominant source. This is supported by cosmological simulations (e.g. Fernández et al. 2012; Joung et al. 2012b;

Nuza et al. 2014), although SN-driven gas may still play an important auxiliary role (Fraternali 2017). Similar inferences can be made for other sufficiently massive galaxies at all redshifts (Putman 2017; Lockman 2017 and references therein).

Theoretically, the classical picture of galaxy formation dictated that most of the collapsing gas is initially shock heated to the virial temperature of the gravitational potential (Rees & Ostriker 1977; Silk 1977; White & Rees 1978); a view that continued after the emergence of the cold dark matter (CDM) cosmology (White & Frenk 1991). However, more recent studies led to the recognition that substantial infall of cold gas can occur via filamentary streams without being shock heated until it reaches the denser regions of the forming galaxy (Birnboim & Dekel 2003; Kereš et al. 2005; Stewart 2017; see also Binney 1977). Such “cold accretion” may be the dominant mode of gas accretion for all galaxies at early epochs, as well as in present-day galaxies with total mass $M \lesssim 10^{12} M_{\odot}$, close to that of the Milky Way (e.g. Brooks et al. 2009; van de Voort et al. 2011; Faucher-Giguère et al. 2011; see however Nelson et al. 2013).

1.2. High velocity clouds and accretion

The most direct evidence of infalling cold gas (with temperature $T \lesssim 10^4$ K) in the Milky Way is provided by high-velocity clouds (HVCs) of neutral hydrogen, observed with line-of-sight (LOS) velocities between -500 and $+450 \text{ km s}^{-1}$ in the local-standard-of-rest frame that deviate strongly from simple expectations for Galactic rotation (Wakker & van Woerden 1997; Putman et al. 2012; Richter 2017). They are found throughout the sky with a range of angular sizes, from $< 2 \text{ deg}$ for compact HVCs (CHVCs) up to $\sim 1500 \text{ deg}^2$ for large HVC complexes, a range of HI col-

¹ Astrophysical Big Bang Laboratory, RIKEN, 2-1 Hirosawa, Wako 351-0198 Japan; susumu.inoue@riken.jp

² Department of Physics, Rikkyo University, 3-34-1 Nishi-Ikebukuro, Toshima-ku, Tokyo 171-8501, Japan

³ Laboratoire Univers et Particules de Montpellier, Université Montpellier, CNRS/IN2P3, CC 72, Place Eugène Bataillon, F-34095 Montpellier Cedex 5, France

⁴ Graduate School of Science and Engineering, 1-21-35 Korimoto, Kagoshima University, Kagoshima 890-0065, Japan

umn densities $N_{\text{HI}} \gtrsim 10^{17} - 10^{20} \text{ cm}^{-2}$, metallicities (relative to solar) $Z/Z_{\odot} \sim 0.1 - 0.5$, and lacking stellar components. While a major fraction of HVCs is known to constitute the Magellanic Stream and the Leading Arm (hereafter collectively MS), likely comprising gas stripped from the Magellanic Clouds (D’Onghia & Fox 2016), the origin of most other HVCs is unclear. Many of the larger complexes have been constrained to reside in the halo, with distances $D \sim 2 - 15 \text{ kpc}$ and HI masses $M_{\text{HI}} \sim 10^5 - 5 \times 10^6 M_{\odot}$, implying mean densities $n_{\text{HI}} \sim 0.1 \text{ cm}^{-3}$ (Putman et al. 2012; Richter 2017). Most HVCs are also known to possess associated, warm ionized gas (with $T \sim 10^4 - 10^5 \text{ K}$) observed in H α or low ionization metal lines, whose total mass may be greater than that in HI (Lehner & Howk 2011; Putman et al. 2012; Richter 2017). HVCs have also been identified in nearby galaxies including M31 and M33 (Lockman 2017, and references therein).

Long suspected to be the fuel reservoir for disk star formation (Oort 1970), the net gas accretion rate due to HVCs is uncertain, and recent estimates vary among different authors. Depending on the treatment of the ionized component and the contribution from the MS, it ranges from $\dot{M}_{\text{acc,HVC}} \sim 0.1 M_{\odot} \text{ yr}^{-1}$ (Putman et al. 2012) to $\dot{M}_{\text{acc,HVC}} \gtrsim 5 M_{\odot} \text{ yr}^{-1}$ (Richter 2017), between falling significantly short to being more than sufficient for the required $\dot{M}_{\text{acc,SF}}$. The dominance of warm ionized gas over HI for accretion appears to be supported by recent cosmological simulations (Joung et al. 2012b; Murante et al. 2012; Nuza et al. 2014). Hydrodynamical simulations suggest that HVCs entering the inner regions of the halo may be substantially disrupted and ablated by interacting with ambient hot gas (at $T \gtrsim 10^6 \text{ K}$) that likely permeates the halo (Spitzer 1956; Bland-Hawthorn & Gerhard 2016), unless their initial gas mass $M \gtrsim 10^{4.5} M_{\odot}$ (Heitsch & Putman 2009; Kwak et al. 2011; Joung et al. 2012a; Armillotta et al. 2017). SN-driven outflows may further disturb HVCs near the disk, although mixing with metal-enriched gas from the former may allow remnant gas from the latter to eventually recool and undergo “quiet” accretion at low velocities (Marinacci et al. 2010; Fraternali 2017).

Direct accretion of “cool” gas with $T \lesssim 10^5 \text{ K}$ (here referring to both cold and warm gas) onto the disk at high velocities is expected to be most important in the outer Galaxy, where HVCs are likely less affected by the hot halo or outflows from the disk driven by SNe or the central supermassive black hole (SMBH; van de Voort 2017). Moreover, gas from all likely sources (IGM, satellites or halo) are more prone to accrete onto the outer disk regions due to their higher angular momenta relative to the disk (Peek 2009; Christensen et al. 2016; Stewart 2017), which may subsequently be transported radially inward to fuel star formation in the central regions (Finlator 2017). This notion may be consistent with various observations (Combes 2014) and cosmological simulations (Stewart et al. 2011; Fernández et al. 2012). Direct collisions of HVCs with the disk have been proposed as the origin of supershells and other large HI structures in the disk that cannot be easily explained by stellar activity or supernovae (Heiles 1984; Tenorio-Tagle & Bodenheimer 1988; Baek et al. 2008), as well as warps and lopsidedness seen in the outer regions of most disk galaxies including the Milky Way (Sancisi et al. 2008; Combes 2014).

A particularly clear example of a direct HVC accretion event was recently discovered by Park et al. (2016). It was initially identified as a faint “forbidden-velocity wing” (FVW),

i.e. localized HI structure in the Galactic disk with velocity deviating from Galactic rotation by more than 20 km s^{-1} (Kang & Koo 2007). Deeper HI observations at higher spatial and spectral resolution revealed a kpc-scale supershell with a CHVC at its center, the former most likely resulting from the impact of the latter with the disk. Park et al. (2016) favor a location in the outer Galaxy at Galactocentric distance $R \sim 15 \text{ kpc}$, and infer initial values for the relative velocity $v \sim 240 \text{ km s}^{-1}$ and HVC mass $M_{\text{HVC}} \gtrsim 6 \times 10^4 M_{\odot}$.

1.3. HVC accretion events and non-thermal phenomena

HVCs striking the disk without much prior deceleration will give rise to forward shocks in the disk gas and/or reverse shocks within the HVC that can be strong depending on the conditions (e.g. Tenorio-Tagle et al. 1986, 1987; Baek et al. 2008). Although the thermal emission from the shocked gas expected in the UV to soft X-ray band is likely difficult to observe, an interesting question is whether such shocks can generate high-energy protons and electrons via diffusive shock acceleration (DSA; e.g. Bell 1978; Blandford & Ostriker 1978) and induce non-thermal emission that may be observable. Of particular interest in this regard are numerous unidentified GeV-TeV gamma-ray sources, many spatially extended, that have been discovered in surveys of the Galactic Plane by H.E.S.S. (Aharonian et al. 2005, 2006), Fermi-LAT (Ackermann et al. 2016, 2017), HAWC (Abeysekara et al. 2017), and other facilities. Although a fair fraction of TeV sources from the first surveys were later revealed to be known types of objects such as supernova remnants (SNRs; Gottschall et al. 2016) or pulsar wind nebulae (PWNe; Abdalla et al. 2017), some have remained mysterious, and new unidentified sources continue to be found with deeper observations (Deil et al. 2015; Donath et al. 2017; see TeVCat⁵). One especially enigmatic source is HESS J1503-582, detected up to $\sim 20 \text{ TeV}$ with spatial extension $\sim 0.5^{\circ}$ (Renaud et al. 2008) and a sub-TeV counterpart (Ackermann et al. 2016). Categorized as a “dark” source in TeVCat with no obvious counterparts at radio, infrared or X-ray bands, Renaud et al. (2008) report a possible association with a FVW of unknown distance and nature, initially discovered by Kang & Koo (2007).

Here we discuss the possibility that shocks driven by HVC accretion events of the kind described above are accelerators of protons and electrons to GeV-TeV energies and consequent sources of non-thermal emission in gamma-rays and other wavebands. Analogous to the FVW that was revealed to be a CHVC-supershell system (Park et al. 2016), we propose that HESS J1503-582 with its associated FVW was triggered by a similar event in the outer Galactic disk, its gamma-rays resulting from neutral pion-decay and inverse Compton emission induced by protons and electrons, respectively. We note that HVCs at high Galactic latitudes not interacting with the disk are undetected in gamma rays, a fact has been used to constrain the amount of cosmic rays (CRs) propagating in the halo (Tibaldo et al. 2015).

The rest of the paper is organized as follows. The next three sections describe basic aspects of physics relevant to HVC accretion events, our assumptions and parameters, and some order-of-magnitude estimates, concerning shock properties in §2, particle acceleration in §3, and non-thermal emission in §4. In §5, the expected non-thermal emission is calculated numerically and compared with observations of the “dark” GeV-

⁵ <http://tevcat.uchicago.edu/>

TeV source HESS J1503-582. Further observational tests and searches for other similar sources with current and future facilities are discussed in §6. We conclude in §7 by touching upon implications for the observed diffuse gamma-ray emission in the outer Galaxy, and prospects for obtaining new insight into gas accretion processes onto galaxies. Most salient points of this work were already presented at the 5th International Symposium on Gamma-Ray Astronomy in 2012, for which the slides are available online ⁶.

2. SHOCK PROPERTIES AND ENERGETICS

2.1. HVCs and the Galactic disk

Key parameters for HVCs are its 3-dimensional velocity that can be characterized by magnitude v_{HVC} and orientation relative to the disk rotation, total gas mass M_{HVC} including both cold and warm ionized components at $T \lesssim 10^5$ K, and mean internal gas density n_{HVC} , just before their impact with the disk. One also needs the distribution of all these variables and their spatial dependence, particularly on Galactocentric distance R , for the population of HVCs. For HI gas in the disk, plausible models are available for the mean radial profiles of circular velocity v_{disk} , density n_{disk} and scale height h_{disk} that are in accord with existing observations (Kalberla & Kerp 2009; Bland-Hawthorn & Gerhard 2016). The mean rotation curve is consistent with being roughly flat at $v_{\text{disk}} \sim 220 \text{ km s}^{-1}$ from the solar circle at $R = R_{\odot} \simeq 8.5$ kpc out to at least $R \sim 20$ kpc, albeit with large observational uncertainties. The HI disk is known to extend significantly beyond the observed stellar disk, possibly up to $R \sim 60$ kpc. The warm ionized gas in the disk may also be relevant, but is not considered here as its surface density is subdominant, especially in the outer Galaxy (Ferrière 2001; Yao et al. 2017). With knowledge of these quantities, we can estimate for each collision the relative velocity v_{acc} between the HVC and the disk, and the mean velocities $v_{s,f}$ and $v_{s,r}$ for the resultant forward shock (FS) in the disk and the reverse shock (RS) in the HVC, respectively. If the cloud's initial gas mass $M \gtrsim 10^{4.5} M_{\odot}$ and/or the location is in the outer Galaxy, HVCs may not be significantly decelerated before disk impact (§1.2), in which case v_{HVC} is expected to be of order v_{disk} , especially for HVCs originating from the IGM or satellites high above the Galactic Plane. Consequently, v_{acc} should also be of the same order.

The actual distribution of the HVC parameters is highly uncertain. Observations only provide the LOS component of the velocity, and are strongly affected by selection effects near the disk. Measurements of M_{HVC} and n_{HVC} are only available for the largest HVCs with distance constraints. Current cosmological simulations do not yet have sufficient resolution to elucidate the detailed physics of the disk-halo interface. In view of the uncertainties, we simply regard as parameters v_{HVC} and v_{acc} with the same fiducial value of 300 km s^{-1} . We also fiducially take $n_{\text{HVC}} = 0.1 \text{ cm}^{-3}$ and $M_{\text{HVC}} = 10^5 M_{\odot}$, the latter above the inferred threshold for HVC survival from disruptive hydrodynamical processes in the halo. Finally, we consider a fiducial impact location at $R = 15$ kpc, where $n_{\text{disk}} \sim 0.1 \text{ cm}^{-3}$ at midplane and $h_{\text{disk}} \sim 300$ pc for the HI disk (Kalberla & Kerp 2009). Our fiducial values are in line with those invoked for the pre-collision CHVC by Park et al. (2016).

2.2. Shock velocity and lifetime

Under the idealized assumption of uniform spherical clouds colliding perpendicularly with a static, uniform slab disk with given v_{acc} , n_{HVC} and n_{disk} , approximate analytic descriptions of the relevant hydrodynamics have been presented by Tenorio-Tagle (1980, 1981). In reality, this only applies in the rare case when the HVC has no radial motion and its azimuthal velocity equals v_{disk} , not to mention further complications in situations with oblique incidence, non-trivial density structure and geometry, etc. Nevertheless, we can expect that both $v_{s,f}$ and $v_{s,r}$ will be of order v_{acc} , as long as $n_{\text{HVC}}/n_{\text{disk}}$ is not greatly different from unity. We consider v_s as a parameter to stand for either $v_{s,f}$ or $v_{s,r}$, again with fiducial value 300 km s^{-1} , bearing in mind that for $v_s \lesssim 120 \text{ km s}^{-1}$, particle acceleration to high energies may be suppressed by non-trivial effects (§3.4). A more detailed description warrants hydrodynamical simulations (e.g. Tenorio-Tagle et al. 1986, 1987; Kudoh & Basu 2004; Baek et al. 2008), which are beyond the scope of this paper.

The sonic Mach number of a shock propagating in gas with temperature T_0 is

$$\mathcal{M}_s = \frac{v_s}{(\gamma k_B T_0 / \mu m_p)^{1/2}} \simeq 20.1 \left(\frac{v_s}{300 \text{ km s}^{-1}} \right) \left(\frac{T_0}{10^4 \text{ K}} \right)^{-1/2}, \quad (1)$$

where k_B is the Boltzmann constant, m_p is the proton mass, and $\gamma = 5/3$ and $\mu = 0.62$ are respectively the adiabatic index and mean molecular weight for fully ionized monatomic gas with solar composition. (The assumption of fully ionized pre-shock gas is justified in §3.4). The disk gas at $R > R_{\odot}$ is suspected to be mainly in the warm neutral phase with $T_0 \sim 6000 - 10^4$ K (Ferrière 2001), so that for HVC-driven FS in this region, $\mathcal{M}_s \sim 20 - 26$ ($v_s/300 \text{ km s}^{-1}$), or higher if the disk gas at the impact location is colder. On the other hand, observed HI line widths of HVCs indicate $T_0 \sim 500 - 9000$ K (Putman et al. 2012), so $\mathcal{M}_s \sim 21 - 90$ ($v_s/300 \text{ km s}^{-1}$) for RS within the cold component of HVCs, while $\mathcal{M}_s \sim 6 - 20$ ($v_s/300 \text{ km s}^{-1}$) for those in the warm ionized component with $T_0 \sim 10^4 - 10^5$ K. Most of this range qualify as strong shocks with compression ratio $r_c = (\gamma + 1)\mathcal{M}_s^2 / [(\gamma - 1)\mathcal{M}_s^2 + 2] \sim 4$, and can be interesting for particle acceleration (§3.3).

The radius of a uniform, spherical HVC is

$$r_{\text{HVC}} = \left(\frac{3M_{\text{HVC}}}{4\pi m_p n_{\text{HVC}}} \right)^{1/3} \simeq 213 \text{ pc} \left(\frac{n_{\text{HVC}}}{0.1 \text{ cm}^{-3}} \right)^{-1/3} \left(\frac{M_{\text{HVC}}}{10^5 M_{\odot}} \right)^{1/3}. \quad (2)$$

Assuming that the shocks remain adiabatic, the approximate crossing time of the RS through the HVC is

$$\tau_{\text{HVC}} \approx \frac{2r_{\text{HVC}}}{v_{s,r}} \simeq 1.4 \times 10^6 \text{ yr} \times \left(\frac{n_{\text{HVC}}}{0.1 \text{ cm}^{-3}} \frac{M_{\text{HVC}}}{10^5 M_{\odot}} \right)^{1/3} \left(\frac{v_s}{300 \text{ km s}^{-1}} \right)^{-1}, \quad (3)$$

⁶ <https://www.mpi-hd.mpg.de/hd2012/pages/presentations/Inoue.pdf>

while that for the FS through the disk is

$$\tau_{\text{disk}} \approx \frac{2h_{\text{disk}}}{v_{s,f} \cos \theta} \approx 2.0 \times 10^6 \text{ yr} \times \frac{1}{\cos \theta} \left(\frac{h_{\text{disk}}}{300 \text{ pc}} \right) \left(\frac{v_s}{300 \text{ km s}^{-1}} \right)^{-1}, \quad (4)$$

where θ is the angle of impact with respect to the disk normal.

The post-shock gas temperature for a strong shock is

$$T_s = \frac{2(\gamma-1)\mu v_s^2}{(\gamma+1)^2 k_B} \approx 1.3 \times 10^6 \text{ K} \left(\frac{v_s}{300 \text{ km s}^{-1}} \right)^2. \quad (5)$$

The thermal emission peaking in the far UV to soft X-ray range could be challenging to observe due to strong photoelectric absorption by the foreground interstellar medium (ISM; §6.4). For gas in collisional ionization equilibrium at constant density n , $10^5 < T < 10^{6.5}$ K and $0.1 < Z/Z_\odot < 1$, the radiative cooling time can be approximated by $\tau_{g,\text{rad}} \sim 1.3 \times 10^5 \text{ yr} (n/1 \text{ cm}^{-3})^{-1} (Z/Z_\odot)^{-0.8} (T/10^6 \text{ K})^{1.7}$ (Draine 2011). The radiative cooling time of the post-shock gas is

$$\tau_{g,\text{rad}} \approx 1.8 \times 10^6 \text{ yr} \times \left(\frac{r_c n_0}{0.4 \text{ cm}^{-3}} \right)^{-1} \left(\frac{Z}{0.2 Z_\odot} \right)^{-0.8} \left(\frac{v_s}{300 \text{ km s}^{-1}} \right)^{3.4}, \quad (6)$$

where n_0 denotes the pre-shock gas density. Note that $Z/Z_\odot \sim 0.1 - 0.3$ is the typical observed metallicity of HVC gas (Putman et al. 2012; Richter 2017), while $Z/Z_\odot \sim 0.2 - 0.3$ for the disk at $R \sim 15$ kpc (Henry & Worthey 1999; Matteucci 2014 and references therein).

The duration of the phase during which the shocks traverse the medium at roughly constant velocity before beginning to decelerate can be estimated by $\tau_s \sim \min[\tau_{\text{disk}}, \tau_{\text{HVC}}, \tau_{g,\text{rad}}]$. If $\tau_{\text{HVC}} < \tau_{\text{disk}} < \tau_{g,\text{rad}}$, the entire HVC is shocked and decelerated by the adiabatic RS before the FS crosses the disk, after which the RS decays and the FS decelerates. If $\tau_{\text{disk}} < \tau_{\text{HVC}} < \tau_{g,\text{rad}}$, the adiabatic FS driven by the HVC emerges from the opposite side of the disk before the cloud is completely shocked, after which the FS decays and the RS decelerates. When $\tau_{g,\text{rad}}$ is shortest timescale, both FS and RS become radiative and start to decelerate before crossing the disk and cloud, respectively. Note that for given v_{acc} , $v_{s,f}$ and $v_{s,r}$ differ by a numerical factor that depends on $n_{\text{HVC}}/n_{\text{disk}}$ (Tenorio-Tagle 1980, 1981), so strictly speaking, τ_{HVC} and τ_{disk} should not be evaluated simultaneously with the same value of v_s . This pre-deceleration phase at constant velocity will be our main focus, even though the ensuing deceleration phase may also be of some interest for particle acceleration (§3.4).

The timescales τ_{disk} , τ_{HVC} , and $\tau_{g,\text{rad}}$ are plotted as functions of v_s in Fig. 1, showing that unless $v_s \gtrsim 300 \text{ km s}^{-1}$ for our fiducial case of $r_c n_0 = 0.4 \text{ cm}^{-3}$, both RS and FS become radiative before crossing their respective media, where particle acceleration is likely less efficient (§3.4). If $r_c n_0 = 4 \text{ cm}^{-3}$, this is unavoidable up to $v_s \sim 500 \text{ km s}^{-1}$.

2.3. Energetics and number

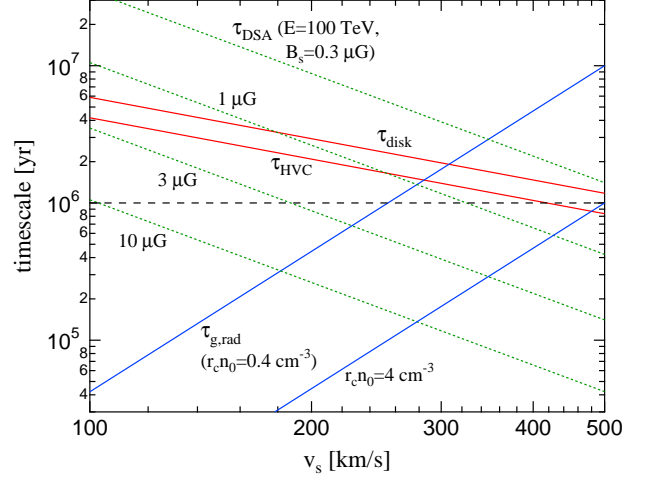


FIG. 1.— Characteristic timescales versus shock velocity v_s . Plotted are the crossing time of the Galactic disk by the forward shock, τ_{disk} (Eq. 4; upper red line), the crossing time of the high velocity cloud by the reverse shock, τ_{HVC} (Eq. 3; lower red line), and the radiative cooling time of the post-shock gas, $\tau_{g,\text{rad}}$, with density $r_c n_0 = 0.4$ and 4 cm^{-3} (Eq. 6; upper and lower blue lines, respectively). Overlaid are the timescales for diffusive shock acceleration, τ_{DSA} , for protons or electrons up to energy $E = 100$ TeV with post-shock magnetic field $B_s = 0.3, 1, 3$ and $10 \mu\text{G}$ (Eq. 12 with $q = 1$; green dashed lines, from top to bottom). The age of $t = 10^6$ yr considered for our models in §5 is also denoted (black long-dashed line).

The kinetic energy of a HVC is

$$\mathcal{E}_{\text{HVC}} = \frac{1}{2} M_{\text{HVC}} v_{\text{HVC}}^2 \approx 9.0 \times 10^{52} \text{ erg} \left(\frac{M_{\text{HVC}}}{10^5 M_\odot} \right) \left(\frac{v_{\text{HVC}}}{300 \text{ km s}^{-1}} \right)^2, \quad (7)$$

which could be up to $\mathcal{E}_{\text{HVC}} \sim 5 \times 10^{54} (v_s/300 \text{ km s}^{-1})^2 \text{ erg}$ for the most massive HVCs. Their significantly larger energy compared to typical SN explosions led them to be recognized as promising energy sources for creating supershells and other large HI structures (Tenorio-Tagle & Bodenheimer 1988). The rate at which this kinetic energy flows into a shock with surface area $A_s = \pi r_s^2 \sim \pi r_{\text{HVC}}^2$ is

$$L_{k,\text{HVC}} \approx \frac{1}{2} m_p n_0 v_s^3 A_s \approx 3.1 \times 10^{39} \text{ erg s}^{-1} \times \left(\frac{n_0}{0.1 \text{ cm}^{-3}} \right) \left(\frac{n_{\text{HVC}}}{0.1 \text{ cm}^{-3}} \right)^{-2/3} \left(\frac{M_{\text{HVC}}}{10^5 M_\odot} \right)^{2/3} \left(\frac{v_s}{300 \text{ km s}^{-1}} \right)^3, \quad (8)$$

where $n_0 = n_{\text{HVC}}$ for the RS and $n_0 = n_{\text{disk}}$ for the FS, and Eq. 2 has been used. For $n_0 = n_{\text{HVC}}$, the expression reduces to $L_{k,\text{HVC}} \approx (3/2)(\mathcal{E}_{\text{HVC}}/\tau_{\text{HVC}})(v_s/v_{\text{HVC}})^2$.

The total power due to all accreting HVCs in the Galaxy with v_{acc} , i.e. the rate at which their kinetic energy is dissipated in the disk, can be estimated as

$$\mathcal{L}_{\text{acc,HVC}} \approx \frac{1}{2} f_{\text{acc}} \dot{M}_{\text{acc,HVC}} v_{\text{acc}}^2 \approx 2.9 \times 10^{40} \text{ erg s}^{-1} f_{\text{acc}} \left(\frac{\dot{M}_{\text{acc,HVC}}}{1 M_\odot \text{ yr}^{-1}} \right) \left(\frac{v_{\text{acc}}}{300 \text{ km s}^{-1}} \right)^2, \quad (9)$$

Some or possibly most of this reflects accretion onto the outer

regions of the disk (§1.2, §6.1). The factor f_{acc} accounts for a number of effects. First, as there must be a distribution in v_{acc} , only a part of $\dot{M}_{\text{acc,HVC}}$ corresponds to direct accretion onto the disk with $v_{\text{acc}} \sim 300 \text{ km s}^{-1}$. Second, some HVCs may penetrate the disk while dissipating only a fraction of their kinetic energy (Tenorio-Tagle et al. 1986, 1987; Baek et al. 2008). A realistic value of f_{acc} is difficult to estimate, but $f_{\text{acc}} \ll 1$ is possible if much of the accretion turns out to proceed quietly with low v_{acc} (e.g. Fraternali 2017). On the other hand, the total power from SNe with kinetic energy \mathcal{E}_{SN} and rate \mathcal{R}_{SN} is

$$\mathcal{L}_{\text{SN}} = \mathcal{E}_{\text{SN}} \mathcal{R}_{\text{SN}} \simeq 9.5 \times 10^{41} \text{ erg s}^{-1} \left(\frac{\mathcal{E}_{\text{SN}}}{10^{51} \text{ erg}} \frac{\mathcal{R}_{\text{SN}}}{0.03 \text{ yr}^{-1}} \right). \quad (10)$$

As is well known, with a plausible CR acceleration efficiency of order 10 % (§3.3), \mathcal{L}_{SN} can account for the energy budget of the observed Galactic CRs with inferred power $\mathcal{L}_{\text{CR}} \sim 10^{41} \text{ erg s}^{-1}$ (Ginzburg & Syrovatskii 1964; Strong et al. 2010; Grenier et al. 2015). In comparison, $\mathcal{L}_{\text{acc,HVC}}$ is only $\sim 3 \%$ of \mathcal{L}_{SN} , and possibly even less if $f_{\text{acc}} \ll 1$. Nevertheless, the energetics of HVC accretion can be relatively more important in the outer Galaxy where \mathcal{R}_{SN} is much lower (§7).

The mean number of active HVC accretion events with adiabatic shocks in the Galaxy can be crudely estimated by

$$N_s \approx f_s (\dot{M}_{\text{acc,HVC}} / M_{\text{HVC}}) \tau_s \\ \simeq 10 f_s \left(\frac{\dot{M}_{\text{acc,HVC}}}{1 M_{\odot} \text{ yr}^{-1}} \frac{\tau_s}{10^6 \text{ yr}} \right) \left(\frac{M_{\text{HVC}}}{10^5 M_{\odot}} \right)^{-1}, \quad (11)$$

Similar to f_{acc} , f_s accounts for the fact that only a fraction of $\dot{M}_{\text{acc,HVC}}$ is represented by accretion of HVCs with $M_{\text{HVC}} \sim 10^5 M_{\odot}$ and $\tau_s \sim 10^6 \text{ yr}$.

The above estimates of $\mathcal{L}_{\text{acc,HVC}}$ and N_s are subject to uncertainties in $\dot{M}_{\text{acc,HVC}}$. Putman et al. (2012) give $\dot{M}_{\text{acc,HVC}} \sim 0.1 - 0.4 M_{\odot} \text{ yr}^{-1}$, including the ionized gas seen in H α , but excluding the contribution from the MS. Estimating the contribution of ionized gas detected via metal lines, Lehner & Howk (2011) derive $\dot{M}_{\text{acc,HVC}} \sim 0.45 - 1.40 M_{\odot} \text{ yr}^{-1}$, which meets the required $\dot{M}_{\text{acc,SF}}$. Finally, accounting for the MS that may potentially dominate accretion for $\sim 1 \text{ Gyr}$, Richter (2012, 2017) give $\dot{M}_{\text{acc,HVC}} \sim 0.7 M_{\odot} \text{ yr}^{-1}$ in HI alone, and a total including ionized gas of $\dot{M}_{\text{acc,HVC}} \gtrsim 5 M_{\odot} \text{ yr}^{-1}$. However, it is unclear if the bulk of the MS can reach the disk without being disrupted (Fox et al. 2014; D’Onghia & Fox 2016). At present, at least a small part of it may be accreting, as some HVCs in the Leading Arm are known to be interacting with the disk at $R \sim 17 \text{ kpc}$ (McClure-Griffiths et al. 2008). Taking the higher value of $\dot{M}_{\text{acc,HVC}}$ by Lehner & Howk (2011), $\mathcal{L}_{\text{acc,HVC}}$ can be up to $\sim 5 \%$ of \mathcal{L}_{SN} .

The threshold mass for HVC survival in the hot halo is also uncertain. While $M_{\text{HVC}} \gtrsim 10^{4.5} M_{\odot}$ is suggested from hydrodynamical simulations for evading disruption via Kelvin-Helmholtz and Rayleigh-Taylor instabilities (Heitsch & Putman 2009; Kwak et al. 2011; Joung et al. 2012a), such effects may be alleviated by inclusion of magnetic fields (McCourt et al. 2015), thermal conduction (Armillotta et al. 2017) or gravitational confinement by dark matter (Nichols & Bland-Hawthorn 2009; Galyardt & Shelton 2016). If direct accretion with high v_{acc}

is also possible for $M_{\text{HVC}} \lesssim 10^{4.5} M_{\odot}$, N_s can be potentially much larger than estimated by Eq. 11. The same is true if we account for shocks in the radiative phase at $\tau_s > 10^6 \text{ yr}$, which may still accommodate some particle acceleration, albeit up to lower energies compared to the adiabatic phase (§3.4).

3. PARTICLE ACCELERATION

Shocks waves are capable of accelerating charged particles to energies far exceeding their thermal values with a power-law energy distribution, as attested by a wide variety of observations, ranging from solar coronal mass ejections to merging clusters of galaxies. Although its theory is far from complete, in general terms, DSA is expected to operate efficiently under the following conditions (for reviews, see e.g. Blandford & Eichler 1987; Malkov & Drury 2001; Blasi 2013; Caprioli 2015).

1. The relevant medium is sufficiently rarefied and magnetized so that shocks form in a collisionless manner, mediated by collective electromagnetic interactions involving plasma instabilities rather than particle collisions (§3.1).
2. An adequate fraction of particles are injected into the acceleration process, usually requiring that either the shock has a sufficiently high Mach number, or there is a sufficiently high density of pre-existing cosmic rays (§3.3).
3. The magnetic field around the shock is sufficiently strong and turbulent over a range of scales so that the injected particles can scatter back and forth across the shock front repeatedly to attain suitably high energies within the available time and/or space constraints (§3.2).
4. The medium is sufficiently ionized so that collisions of ions with neutral particles do not damp such magnetic turbulence (§3.4).

3.1. Magnetic fields

The properties of magnetic fields at the shocks of our interest are uncertain, for both RS in HVCs or FS in the outer Galactic disk. Models of the Galactic magnetic field that are consistent with observed Faraday rotation measures and Galactic synchrotron emission (for reviews, see Haverkorn 2015; Beck 2016) suggest total field strengths $B \sim 1 - 3 \mu\text{G}$ for the disk around $R \sim 15 \text{ kpc}$, with appreciable variations depending on the exact location relative to the spiral arms (e.g. Jansson & Farrar 2012; Beck et al. 2016; Adam et al. 2016). Only 2 HVCs have published measurements of magnetic fields via Faraday rotation at levels of $B \sim 6 - 8 \mu\text{G}$, subject to a number of assumptions concerning the foreground, magnetic field geometry, ionized gas distribution, etc. (McClure-Griffiths et al. 2010; Hill et al. 2013). These particular HVCs may be rather anomalous in having likely passed through the disk (McClure-Griffiths et al. 2010) or possessing an unusually high metallicity (Fox et al. 2016), pointing to the possibility that more typical HVCs have weaker fields that are not readily detectable with existing instrumentation. The general presence of metals in HVCs indicate that they are likely magnetized at some level, although perhaps less so than in the disk due to the lack of Galactic dynamo effects.

If the pre-shock magnetic field with strength B_0 is randomly and isotropically tangled, compression will lead to a post-shock field strength B_s enhanced by a factor $[(r_c^2 + 2)/3]^{1/2}$, whereas if it is coherent, this factor will depend on its orientation with respect to the shock. Furthermore, magnetic fields around the shock may possibly be amplified up to near-equipartition values by CR-induced insta-

bilities if the shock's Alfvénic Mach number \mathcal{M}_A is sufficiently high (Bell 2004; Caprioli 2015), where $\mathcal{M}_A = v_s/v_A \simeq 11 (v_s/300 \text{ km s}^{-1})(B_0/3 \mu\text{G})^{-1}(n_0/0.1 \text{ cm}^{-3})^{1/2}$, and $v_A = B_0/(4\pi\mu m_p n_0)^{1/2}$ is the Alfvén velocity in the pre-shock medium. Although observationally supported for SNR shocks (Uchiyama et al. 2007), the efficiency of such instabilities is unclear for the lower velocity shocks of interest here. In our context, the strength of magnetic fields in equipartition with the CR pressure at the shock can be estimated by $B_{s,\text{eq}}^2/(8\pi) = (1/2)\xi_p m_p n_0 v_s^2$ so that $B_{s,\text{eq}} \simeq 14 \mu\text{G} (\xi_p/0.1)^{1/2}(n_0/0.1 \text{ cm}^{-3})^{1/2}(v_s/300 \text{ km s}^{-1})$, where ξ_p is the fraction of kinetic energy flowing into the shock that is imparted to CR protons (see §3.3 for more details). Given all these uncertainties, we take the post-shock field strength as a parameter with a fiducial value of $B_s = 3 \mu\text{G}$, bearing in mind that higher values up to a limit of $B_{s,\text{eq}}$ may be possible.

With such values of the magnetic field around the shock, it is straightforward to show that for protons carrying the bulk of the pre-shock kinetic energy, the thermalization time via Coulomb collisions is much longer than the gyration timescale over which thermalization via electromagnetic instabilities is believed to be effective (Draine 2011). Condition 1 (collisionless shock) is thus satisfied.

3.2. Acceleration time and maximum energy

The gyroradius of a relativistic particle with charge q and energy E is $r_g = E/qeB \simeq 3.6 \times 10^{-4} \text{ pc} (E/q/\text{TeV})(B/3 \mu\text{G})^{-1}$. In terms of v_s and B_s , the timescale for DSA of particles up to E can be expressed

$$\tau_{\text{DSA}} \approx \frac{10}{3} \frac{\eta c E}{q e B_s v_s^2} \simeq 3.9 \times 10^3 \text{ yr} \times \eta \left(\frac{E/q}{1 \text{ TeV}} \right) \left(\frac{B_s}{3 \mu\text{G}} \right)^{-1} \left(\frac{v_s}{300 \text{ km s}^{-1}} \right)^{-2}, \quad (12)$$

where $\eta \geq 1$ is a factor that depends on r_c , the geometry of magnetic fields on large scales, and the amplitude and spectrum of magnetic turbulence on small scales. For SNR shocks, observations point to $\eta \sim 1$ (e.g. Uchiyama et al. 2007), corresponding to Bohm-limit diffusion in fully turbulent fields. This can be a natural consequence of the resonant streaming instability induced by the CRs (Bell 1978), not necessarily involving magnetic field amplification. We assume that η is not significantly larger than unity, so that condition 3 (turbulent magnetic fields) is not too far from optimal for DSA. The DSA timescale for magnetic fields in the range $B_s = 0.3 - 10 \mu\text{G}$ as a function of v_s is shown in Fig. 1. The maximum energy attained by protons or ions during the constant velocity phase can be evaluated by $\tau_{\text{acc}} = \tau_s$,

$$E_{q,\text{max}} \approx \frac{3}{10} \frac{q e B_s v_s^2 \tau_s}{\eta c} \simeq 256 \text{ TeV} \frac{q}{\eta} \left(\frac{B_s}{3 \mu\text{G}} \frac{\tau_s}{10^6 \text{ yr}} \right) \left(\frac{v_s}{300 \text{ km s}^{-1}} \right)^2. \quad (13)$$

In contrast, acceleration of electrons is limited by radiative

losses on a timescale

$$\tau_{e,\text{rad}} = (\tau_{\text{syn}}^{-1} + \tau_{\text{IC}}^{-1})^{-1} = \frac{3m_e^2 c^3}{4\sigma_T(u_B + u_{\text{ph}})E_e} \simeq 5.2 \times 10^5 \text{ yr} \left(\frac{E_e}{\text{TeV}} \right)^{-1} \left(\frac{u_B + u_{\text{ph}}}{0.6 \text{ eV cm}^{-3}} \right)^{-1}, \quad (14)$$

where $\tau_{\text{syn}} = 3m_e^2 c^3 / 4\sigma_T u_B E_e$ and $\tau_{\text{IC}} = 3m_e^2 c^3 / 4\sigma_T u_{\text{ph}} E_e$ are respectively the energy loss times of an electron with energy E_e due to synchrotron and Thomson-regime inverse Compton (IC) radiation, c is the speed of light, m_e is the electron mass, σ_T is the Thomson cross section, $u_B = B^2/8\pi = 0.224 \text{ eV cm}^{-3} (B_s/3 \mu\text{G})^2$, and u_{ph} is the energy density of IC seed photons (Rybicki & Lightman 1979). Their maximum energy is given by $\tau_{\text{acc}} = \tau_{e,\text{rad}}$ with $q = 1$,

$$E_{e,\text{max}} \approx \frac{3m_e c v_s}{2} \left(\frac{e B_s}{10\eta(u_B + u_{\text{ph}})} \right)^{1/2} \simeq 11.5 \text{ TeV} \times \eta^{-1/2} \left(\frac{B_s}{3 \mu\text{G}} \right)^{1/2} \left(\frac{u_B + u_{\text{ph}}}{0.6 \text{ eV cm}^{-3}} \right)^{-1/2} \left(\frac{v_s}{300 \text{ km s}^{-1}} \right). \quad (15)$$

Note that $u_{\text{ph}} = u_{\text{CMB}} + u_{\text{ISRF}}$ comprises contributions from the cosmic microwave background (CMB) with $u_{\text{CMB}} \simeq 0.26 \text{ eV cm}^{-3}$, and the interstellar radiation field (ISRF) with u_{ISRF} . The latter depends on the location in the Galaxy and is expected to be $u_{\text{ISRF}} \simeq 0.1 \text{ eV cm}^{-3}$ at $R \simeq 15 \text{ kpc}$ (Porter et al. 2008, §5.2). Although part of the IC losses with the ISRF may actually be in the Klein-Nishina regime (§4.2), the associated modification to Eq. 15 should be minor, due to the persistence of Thomson-regime IC losses with the CMB as well as synchrotron losses.

Fig. 2 compares $E_{p,\text{max}}$ (Eq. 13 with $q = 1$) and $E_{e,\text{max}}$ as functions of B_s in the range $0.3 - 10 \mu\text{G}$. Note that in contrast to $E_{p,\text{max}}$ that increases monotonically in proportion to B_s , the dependence of $E_{e,\text{max}}$ on B_s is much weaker. Moreover, $E_{e,\text{max}}$ increases with B_s up to $E_{e,\text{max}} \simeq 12 \text{ TeV}$ at $B_s \sim 3.8 \mu\text{G}$, but decreases beyond due to the onset of synchrotron-dominant losses.

3.3. Acceleration efficiency and spectrum

The acceleration efficiency, i.e. the fraction of energy that is channeled into accelerated particles by the DSA mechanism, is determined by physical processes that are not yet fully understood. For accelerated protons, various observations and some numerical simulations indicate that their total energy can be up to $\sim 10 - 20 \%$ of the pre-shock kinetic energy, as long as $\mathcal{M}_s \gtrsim 10$ (Ackermann et al. 2013; Kang & Ryu 2013; Caprioli 2015 and references therein). As discussed in §2.2, the latter should be valid in most cases for the shocks considered here, justifying condition 2 (adequate shock Mach number). Also governed by \mathcal{M}_s is the spectrum of accelerated particles, expected to be a simple power law in particle momentum p to first order of approximation, $dN/dp \propto p^{-\alpha}$, with index $\alpha = (r_c + 2)/(r_c - 1) = (3\gamma - 1 + 4\mathcal{M}_s^{-2})/(2 - 2\mathcal{M}_s^{-2})$ that approaches $\alpha = 2$ for $\mathcal{M}_s \gtrsim 10$. We assume that during the pre-deceleration, constant velocity phase of the shock with duration τ_s , non-thermal protons with momenta $p \geq p_{p,\text{min}}$ are injected into the emission region at a constant rate

$$Q_p(p) \equiv \frac{dN_p}{dp dt} = Q_{p0} \left(\frac{p}{p_0} \right)^{-\alpha} \exp\left(-\frac{p}{p_{p,\text{max}}}\right) \quad (16)$$

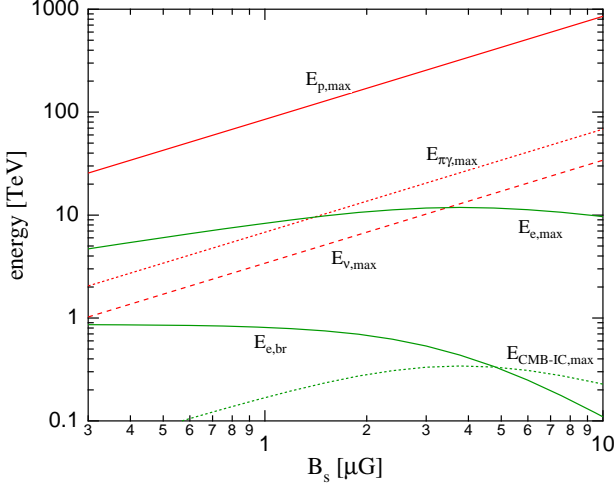


FIG. 2.— Characteric particle and photon energies versus post-shock magnetic field B_s . Compared are maximum energies of protons $E_{p,\max}$ (Eq. 13 with $q = 1$; red solid line) and electrons $E_{e,\max}$ (Eq. 15; upper green solid curve), assuming an interstellar radiation field with $u_{\text{ISRF}} \simeq 0.1 \text{ eV cm}^{-3}$ as appropriate for $R \simeq 15 \text{ kpc}$. Also shown are the maximum energies of pp collision-induced gamma-rays $E_{\pi\gamma,\max} = 0.08 E_{p,\max}$ (red dashed line) and neutrinos $E_{\nu,\max} = 0.04 E_{p,\max}$ (red long-dashed line), the electron cooling break energy $E_{e,\text{br}}$ (Eq. 21; lower green solid curve), and the maximum energy of inverse Compton photons via upscattering of the cosmic microwave background (Eq. 23; green dashed curve).

where $Q_p(p)dp$ denotes the number of protons with momenta in the interval $p \sim p+dp$ injected per unit time, $p_0 = 1 \text{ GeV}/c$, and $\alpha = 2$ is fiducially considered. The minimum momentum of protons is expected to be not far above their thermal values, for which we choose $p_{p,\min} = 0.01 \text{ GeV}/c$, while $p_{p,\max} = E_{p,\max}/c$ is evaluated from Eq. 13. The normalization parameter Q_{p0} is treated differently depending on the objective, in relation to the total power of injected protons $L_p = \int_{p_{p,\min}}^{p_{p,\max}} E_k Q_p(p) dp$ where $E_k = m_p c^2 (\sqrt{((p/m_p c)^2 + 1)} - 1)$ is the proton kinetic energy, or the time-integrated total proton energy $W_p \approx L_p \tau_s$. For giving predictions, Q_{p0} can be set so that $L_p = \xi_p L_{k,\text{HVC}}$, proportional to the rate of HVC kinetic energy passing through the shock (Eq. 8, §2.3), with fiducial value $\xi_p = 0.1$. On the other hand, for providing model fits to observations, Q_{p0} can be adjusted to give the best description of the data, and the corresponding L_p or W_p is evaluated a posteriori for a plausibility check. We do not consider effects that can induce deviations from a simple power-law for the accelerated particle spectrum such as non-linear feedback from CRs onto the shock structure (Malkov & Drury 2001), nor the effects of pre-existing CRs for DSA injection, which is likely subdominant for the conditions of our interest.

Primary electrons, i.e. those directly accelerated out of the thermal plasma via DSA, are treated in a way similar to protons (Eq. 16) with the same value of α so that their injection rate with momenta $p_e \geq p_{e,\min}$ is

$$Q_e(p_e) \equiv \frac{dN_e}{dp_e dt} = Q_{e0} \left(\frac{p_e}{p_0} \right)^{-\alpha} \exp\left(-\frac{p_e}{p_{e,\max}}\right) \quad (17)$$

where $p_{e,\max} = E_{e,\max}/c$ is evaluated from Eq. 15. The minimum momentum of electrons is uncertain but its exact value is not crucial for our purposes as long as $p_{e,\min} \ll 1 \text{ GeV}/c$, where the corresponding synchrotron and IC emission is observationally irrelevant (§4.2); here we take $p_{e,\min} = 0.01 \text{ GeV}/c$.

The electron acceleration efficiency ξ_e , defined so that the total injected electron power $L_e = \xi_e L_{k,\text{HVC}}$, is more uncertain compared to protons, either observationally or theoretically. Often invoked for the ratio of accelerated electrons to protons is $K_{ep} \simeq 0.01$ in terms of their number at momentum $\sim 1 \text{ GeV}/c$, the value observed in Galactic CRs. However, it is unclear how much this reflects the ratio at the acceleration site. Observations of SNRs and some simulations indicate it may be appreciably less (Ackermann et al. 2013; Caprioli 2015), while observations of cluster merger shocks and related simulations suggest that it can be much higher (Guo et al. 2014). We fiducially take $K_{ep} = Q_{e0}/Q_{p0} = 0.01$, but remain open to significantly different values.

3.4. Neutral particles and radiative regime

If the medium around the shock contains a sufficiently large fraction of neutral particles, their collisions with ions can damp the magnetic turbulence that is essential for the DSA process and curtail it (Bell 1978; Drury et al. 1996). For both RS in HVCs and FS in the disk, a major fraction of the pre-shock gas should be HI. On the other hand, irrespective of the pre-shock ionization state, shocks in the radiative regime can keep the upstream gas fully ionized via UV photons from the downstream gas, as long as $v_s \gtrsim 120 \text{ km s}^{-1}$ (Shull & McKee 1979; Hollenbach & McKee 1989). While our main concern is the adiabatic phase of the shocks, $\tau_{g,\text{rad}}$ was seen to be comparable to τ_{HVC} or τ_{disk} with our fiducial parameters (§2.2). Thus, unless we consider the earliest phases of their evolution, our shocks are expected to be at least moderately radiative, likely substantially mitigating the effects of neutral particles. Here we assume the validity of condition 4 (negligible damping of magnetic turbulence by neutral-ion collisions), and defer a more detailed discussion to the future. For the same reason, we do not consider in this work the effects of charge exchange reactions that may lead to non-trivial consequences (e.g. Ohira 2012; Morlino et al. 2013).

We note that particle acceleration may also continue in the radiative phase, possibly with a spectral break above a few GeV when $v_s \lesssim 120 \text{ km s}^{-1}$, as proposed in order to explain some observations of old SNRs and other objects (e.g. Bykov et al. 2000; Yamazaki et al. 2006; Malkov et al. 2011; Lee et al. 2015; Inoue et al. 2017). However, such effects are not yet understood in detail and will not be discussed here.

4. NON-THERMAL EMISSION

For detailed calculations of non-thermal emission and application to unidentified Galactic GeV-TeV sources in §5, we employ a numerical code used in Uchiyama et al. (2010), based on a time-dependent kinetic description of the non-thermal proton and electron populations within a suitable emission region. For protons, the code accounts for their inelastic collisions with ambient matter and consequent pion production, emission due to decay of neutral pions (π^0), and injection of secondary electrons and positrons (e^\pm ; hereafter simply “secondary electrons” unless otherwise noted) due to decay of charged pions (π^\pm). The contribution of helium and other heavy nuclei is accounted for by the nuclear enhancement factor (Mori 2009; Kachelriess et al. 2014), for which we adopt $\epsilon_M = 2.0$ (see §4.1 for more details). For both primary and secondary electrons, the code includes bremsstrahlung with ambient matter, synchrotron emission in magnetic fields, and inverse Compton emission by upscattering the CMB and ISRF with proper account of the Klein-

Nishina regime. For simplicity, the ISRF spectrum is described by two diluted black-body components with temperature and normalization for each chosen so as to approximate the detailed calculations by Porter et al. (2008) of the optical starlight and far-infrared dust emission that depend on R . The proton and electron distributions are calculated self-consistently in a time-dependent way including the effect of energy losses due to all of the above processes.

Below we provide a simplified discussion of the key emission processes, for the sake of estimates and understanding of the numerical results. Readers familiar with the basics of non-thermal emission may skip the rest of this section and move to §5.

4.1. Emission induced by protons

Inelastic collisions of relativistic protons with stationary protons and nuclei in ambient matter lead to production of mainly pions, partitioned roughly equally among π^0 , π^+ and π^- , of which the π^0 decay to gamma-rays, and the π^\pm decay to neutrinos and e^\pm . For a proton with sufficiently high energy E_p , the mean energy of the produced gamma rays and neutrinos are $E_\gamma \approx 0.08 E_p$ and $E_\nu \approx 0.04 E_p$, respectively. The total inelastic pp cross section at $E_p > 10$ GeV can be approximated by $\sigma_{pp} \simeq 3 \times 10^{-26} \text{cm}^2 [0.95 + 0.06 \ln(E_p/\text{GeV})]$, which increases logarithmically with E_p (Aharonian 2004; Dermer & Menon 2009). The relevant energy loss timescale for a proton with $E_p \sim 100$ TeV is

$$\tau_{pp} \approx (n_t \kappa_{pp} \sigma_{pp} c)^{-1} = 1.1 \times 10^8 \text{ yr} \left(\frac{r_c n_0}{0.4 \text{ cm}^{-3}} \right)^{-1}, \quad (18)$$

where $\kappa_{pp} \simeq 0.5$ is the average inelasticity of the pp collision, and the main target matter is considered to be the post-shock gas. The resulting gamma-ray spectrum rises with E_γ abruptly at $E_\gamma \lesssim E_\pi = m_\pi c^2/2 \simeq 67.5$ MeV where m_π is the π^0 mass, mirrors that of the parent protons with similar spectral index, $dN_{\gamma,pp}/dE_\gamma \propto E_\gamma^{-\alpha}$, at $E_\pi \lesssim E_\gamma \lesssim E_{\pi\gamma,\text{max}} \approx 0.08 E_{p,\text{max}}$, and cuts off at $E_\gamma \gtrsim E_{\pi\gamma,\text{max}}$.

At relativistic energies, the proton injection rate is well described by $dN_p/dE_p dt \propto E_p^{-\alpha}$. When $\alpha \simeq 2$, the total proton power can be approximated by $L_p = \int_{E_{p,\text{min}}}^{E_{p,\text{max}}} E_p (dN_p/dE_p dt) dE_p$, with $E_{p,\text{min}} \sim 1$ GeV and $E_{p,\text{max}}$ given by Eq. 13. Assuming no escape of protons from the emission region, an estimate for the gamma-ray energy flux around $E_\gamma \sim 8$ TeV from a source at distance D is (e.g. Drury et al. 1994; Murase et al. 2008)

$$\begin{aligned} E_\gamma^2 \frac{dN_{\gamma,pp}}{dE_\gamma} &\approx \frac{1}{3} E_p^2 \frac{dN_p}{dE_p dt} \frac{\epsilon_M \min[1, f_{pp}]}{4\pi D^2} \\ &\simeq 3.2 \times 10^{-12} \text{ erg cm}^{-2} \text{ s}^{-1} \left(\frac{C_p}{0.08} \frac{\xi_p L_{k,\text{HVC}}}{3.1 \times 10^{38} \text{ erg s}^{-1}} \frac{\tau_s}{10^6 \text{ yr}} \right) \\ &\quad \times \left(\frac{\epsilon_M}{2.0} \frac{r_c n_0}{0.4 \text{ cm}^{-3}} \right) \left(\frac{D}{20 \text{ kpc}} \right)^{-2}, \quad (19) \end{aligned}$$

where $f_{pp} = \tau_s/\tau_{pp} \simeq 0.0093(r_c n_0/0.4 \text{ cm}^{-3})(\tau_s/10^6 \text{ yr})$ at $E_p \simeq 100$ TeV, $C_p = \ln(E_{p,\text{max}}/E_{p,\text{min}})^{-1}$, and the numerical expression is for our fiducial parameters with $\alpha = 2$ and $E_{p,\text{max}} \simeq 256$ TeV (Eq. 13). The flux in the range $E_\pi \lesssim E_\gamma \lesssim E_{\pi\gamma,\text{max}}$ should be similar for $\alpha = 2$. Such values are typical for the numerous TeV sources found in the H.E.S.S. Galactic Plane Survey (§5.1).

The nuclear enhancement factor ϵ_M takes into account the additional contribution to pion production by He and heavier nuclei, both in the CRs and in the target matter. For Galactic CRs impinging on gas with solar composition, Mori (2009) gives $\epsilon_M = 1.84$ for CR kinetic energy of 10 GeV/nucleon, slowly increasing to $\epsilon_M = 2.00$ for 1 TeV/nucleon. In our case, the main energy of interest is still higher, while the abundance of nuclei heavier than C are likely much lower in the CRs and target gas. Further uncertainties concern details of hadronic interactions (Kachelriess et al. 2014) and relative spectral variance among CR species near the source that may differ from Galactic CRs. In view of the ambiguities, we choose $\epsilon_M = 2.0$ for simplicity, noting that a precise value is not critical for our aims.

The co-produced neutrino flux per flavor at $E_\nu \approx 0.04 E_p$ is approximately 1/2 of Eq. 19. Considering $E_p \sim 250$ TeV, the flux at $E_\nu \simeq 10$ TeV is

$$\begin{aligned} E_\nu^2 \frac{dN_{\nu,pp}}{dE_\nu} &\approx \frac{1}{6} E_p^2 \frac{dN_p}{dE_p dt} \frac{\epsilon_M \min[1, f_{pp}]}{4\pi D^2} \\ &\simeq 1.8 \times 10^{-12} \text{ erg cm}^{-2} \text{ s}^{-1} \left(\frac{C_p}{0.08} \frac{\xi_p L_{k,\text{HVC}}}{3.1 \times 10^{38} \text{ erg s}^{-1}} \frac{\tau_s}{10^6 \text{ yr}} \right) \\ &\quad \times \left(\frac{\epsilon_M}{2.0} \frac{r_c n_0}{0.4 \text{ cm}^{-3}} \right) \left(\frac{D}{20 \text{ kpc}} \right)^{-2}, \quad (20) \end{aligned}$$

where the numerical expression is for our fiducial parameters with $\alpha = 2$. This may be beyond the capability of current neutrino observatories such as IceCube, but within reach of future facilities (§6.5).

4.2. Emission induced by electrons

Primary electrons of sufficiently high energy can cool efficiently within the available time due to synchrotron and IC losses, leading to a break in their energy distribution relative to $dN_e/dE_e \propto E_e^{-\alpha}$ above the energy where $\tau_{e,\text{rad}} = \tau_s$,

$$E_{e,\text{br}} \approx \frac{3m_e^2 c^3}{4\sigma(u_B + u_{\text{ph}})\tau_s} \simeq 0.52 \text{ TeV} \left(\frac{u_B + u_{\text{ph}}}{0.6 \text{ eV cm}^{-3}} \frac{\tau_s}{10^6 \text{ yr}} \right)^{-1}, \quad (21)$$

where the expression for IC losses in the Thomson regime has been used (§3.2). If $E_{e,\text{br}} > E_{e,\text{max}}$, $dN_e/dE_e \propto E_e^{-\alpha}$ is maintained up to $E_e \sim E_{e,\text{max}}$. Fig. 2 shows $E_{e,\text{br}}$ as a function of B_s when $u_{\text{ISRF}} \simeq 0.1 \text{ eV cm}^{-3}$.

An electron with given E_e radiates synchrotron photons with characteristic energy $E_{\text{sy}} = \epsilon_B (E_e/m_e c^2)^2$, where $\epsilon_B = 3heB/4\pi m_e c^2$ and h is the Planck constant (Rybicki & Lightman 1979). When $E_{e,\text{br}} < E_{e,\text{max}}$, the synchrotron spectrum is characterized by $dN_{\gamma,\text{sy}}/dE_\gamma \propto E_\gamma^{-(\alpha+1)/2}$, becoming steeper at $E_{\text{sy,br}} \lesssim E_\gamma \lesssim E_{\text{sy,max}}$ and cutting off at $E_\gamma \gtrsim E_{\text{sy,max}}$, where $E_{\text{sy,br}} = \epsilon_B (E_{e,\text{br}}/m_e c^2)^2$ and

$$\begin{aligned} E_{\text{sy,max}} &= \epsilon_B (E_{e,\text{max}}/m_e c^2)^2 \\ &\simeq 26 \text{ eV } \eta^{-1} \left(\frac{B_s}{3 \mu\text{G}} \frac{v_s}{300 \text{ km s}^{-1}} \right)^2 \left(\frac{u_B + u_{\text{ph}}}{0.6 \text{ eV cm}^{-3}} \right)^{-1}. \quad (22) \end{aligned}$$

As $B_s < B_{s,\text{eq}} \simeq 14 \mu\text{G}$ (§3.1), the primary synchrotron spectrum cannot extend beyond the far UV band, implying that HVC accretion events may not be readily detectable in X-rays (§5.3, §6.3). This is in stark contrast to SNRs or PWNe for

which $E_{\text{sy,max}}$ is generally at X-ray energies or higher, due to their much higher shock velocities and/or magnetic fields.

Up-scattering of seed photons with energy ϵ_0 by an electron with given E_e results in IC photons with characteristic energy $E_{\text{IC}} = \epsilon_0(E_e/m_e c^2)^2$ when it occurs in the Thomson regime, corresponding to $E_e \ll (m_e c^2)^2/\epsilon_0 \simeq 410 \text{ TeV}(\epsilon_0/\epsilon_{\text{CMB}})^{-1} \simeq 0.26 \text{ TeV}(\epsilon_0/\epsilon_{\text{star}})^{-1}$, where $\epsilon_{\text{CMB}} \simeq 6.4 \times 10^{-4} \text{ eV}$ and $\epsilon_{\text{star}} \simeq 1 \text{ eV}$ are typical photon energies for the CMB and the starlight component of the ISRF, respectively. When $E_e \gtrsim (m_e c^2)^2/\epsilon_0$, scattering proceeds in the Klein-Nishina regime where the relation between E_{IC} and E_e is not as simple, other than the limit $E_{\text{IC}} < E_e$. With our fiducial parameters, electrons with $E_e = E_{e,\text{br}}$ are in the Thomson regime for either CMB or ISRF so that the associated IC photon energy is $E_{\text{IC,br}} = \epsilon_0(E_{e,\text{br}}/m_e c^2)^2$. On the other hand, electrons with $E_e = E_{e,\text{max}}$ are in the Thomson regime only for the CMB, for which the IC photon energy

$$E_{\text{IC,max}} = \epsilon_0(E_{e,\text{max}}/m_e c^2)^2 \simeq 0.32 \text{ TeV} \eta^{-1} \times \left(\frac{\epsilon_0}{\epsilon_{\text{CMB}}} \right) \left(\frac{B_s}{3 \mu\text{G}} \right) \left(\frac{v_s}{300 \text{ km s}^{-1}} \right)^2 \left(\frac{u_B + u_{\text{ph}}}{0.6 \text{ eV cm}^{-3}} \right)^{-1}, \quad (23)$$

which is plotted in Fig. 2 as a function of B_s when $u_{\text{ISRF}} \simeq 0.1 \text{ eV cm}^{-3}$. For the ISRF starlight, such electrons are in the Klein-Nishina regime instead, so that $E_{\text{IC,max}}$ is limited by $E_{e,\text{max}} \lesssim 12 \text{ TeV}$ (§3.2, Fig. 2). When $E_{e,\text{br}} < E_{e,\text{max}}$, the IC spectrum is analogous to that for synchrotron, with $dN_{\gamma,\text{IC}}/dE_{\gamma} \propto E_{\gamma}^{-(\alpha+1)/2}$ at $E_{\gamma} \lesssim E_{\text{IC,br}}$, becoming steeper at $E_{\text{IC,br}} \lesssim E_{\gamma} \lesssim E_{\text{IC,max}}$ and cutting off at $E_{\gamma} \gtrsim E_{\text{IC,max}}$, except that the break and cutoff features are broader from the convolution over the seed photon spectra of both CMB and ISRF, and the cutoff is also steeper due to Klein-Nishina effects.

At relativistic energies, the injection rate for electrons is K_{ep} times that for protons evaluated at the same energy, $(dN_e/dE_e dt)|_{E_e=E} = K_{ep}(dN_p/dE_p dt)|_{E_p=E}$. The steady-state distribution of electrons at $E_e \lesssim E_{e,\text{br}}$ should be roughly unchanged from the injected distribution, $\tau_s(dN_e/dE_e dt)$. Considering only the CMB as seed photons, the IC energy flux at $E_{\gamma} < E_{\text{IC,br}}$ can be estimated by substituting $E_e = (E_{\gamma}/\epsilon_{\text{CMB}})^{1/2} m_e c^2$ in

$$E_{\gamma}^2 \frac{dN_{\gamma,\text{IC}}}{dE_{\gamma}} \approx \frac{1}{2} E_e^2 \frac{dN_e}{dE_e dt} \frac{\tau_s}{\tau_{\text{IC}}(E_e) 4\pi D^2} \simeq 1.4 \times 10^{-12} \text{ erg cm}^{-2} \text{ s}^{-1} \left(\frac{E_{\gamma}}{\text{GeV}} \right)^{1/2} \times \left(\frac{K_{ep}}{0.01} \frac{C_p}{0.08} \frac{\xi_p L_{k,\text{HVC}}}{3.1 \times 10^{38} \text{ erg s}^{-1}} \frac{\tau_s}{10^6 \text{ yr}} \right) \left(\frac{D}{20 \text{ kpc}} \right)^{-2} \quad (24)$$

(e.g. Dermer & Menon 2009), where the numerical expression is for our fiducial parameters with $\alpha = 2$, somewhat less than the estimated π^0 gamma-ray flux (Eq. 19).

Although the above estimate is for primary electrons only, depending on the value of K_{ep} , the synchrotron and IC emission from secondary e^{\pm} induced by pp collisions can be non-negligible, and in some cases even dominant over primary electrons for certain energy bands (§5.3).

5. HVC ACCRETION ORIGIN OF HIGH-ENERGY GAMMA-RAY SOURCES

5.1. Unidentified Galactic GeV-TeV Sources and HESS J1503-582

Observations of the Galactic Plane in TeV gamma rays over the past decades have revealed numerous sources that are spatially extended on scales $\sim 0.03 - 0.3^\circ$ and lack obvious counterparts at other wavelengths. After the first object found by HEGRA (Aharonian et al. 2002), dozens of such sources were discovered in the inner Galactic Plane Survey (GPS) conducted by H.E.S.S. at Galactic latitudes $|b| < 5^\circ$ with angular resolution $\sim 0.07^\circ$ (Aharonian et al. 2005, 2006, 2008). New sources in this class are continuing to be found in deeper and more extended surveys by H.E.S.S. (Deil et al. 2015; Donath et al. 2017), and in ongoing surveys by the recently completed HAWC array (Abeysekara et al. 2017). Similar sources have also been reported by MILAGRO (Abdo et al. 2007), ARGO (Bartoli et al. 2013), VERITAS (Weinstein et al. 2009) and MAGIC (Aleksić et al. 2014). As of August 2017, TeVCat (Wakely & Horan 2008) lists ~ 55 sources located within $\sim 10^\circ$ of the Galactic Plane with type ‘‘unidentified’’.

A fair number of unidentified sources along the Galactic Plane have also been uncovered in all-sky surveys at GeV energies, most recently by Fermi-LAT. In the 2FHL catalog based on data at 50 GeV - 2 TeV with angular resolution $\sim 0.1^\circ$, 22 sources at $|b| < 10^\circ$ are listed without obvious identification (Ackermann et al. 2016). The Fermi Galactic Extended Source Catalog reveals 8 sources newly detected above 10 GeV with extension $\gtrsim 0.3^\circ$ that are not clearly associated with known objects (Ackermann et al. 2017).

The origin of such unidentified Galactic GeV-TeV sources has been debated, with various proposed explanations including old SNRs (Yamazaki et al. 2006), middle-aged PWNe (de Jager et al. 2009), gamma-ray burst remnants (Atoyan et al. 2006; Ioka & Mészáros 2010), etc. After dedicated follow-up studies across the electromagnetic spectrum, a major fraction of TeV sources that initially lacked identification have later been recognized as known types of objects, especially PWNe (Abdalla et al. 2017) and SNRs (Gottschall et al. 2016).

A unique source that has defied clarification and remains mysterious is HESS J1503-582 (Renaud et al. 2008). Located at Galactic coordinates $(l, b) \sim (319.7^\circ, 0.3^\circ)$ and spatially extended with root mean square size $\sim 0.26^\circ$, its spectrum at 1.3 - 22 TeV can be fit by a power-law with photon index $\Gamma_{\text{HESS}} = 2.4 \pm 0.6$ and flux normalization at 1 TeV of $(1.6 \pm 0.6) \times 10^{-12} \text{ cm}^{-2} \text{ s}^{-1} \text{ TeV}^{-1}$. A counterpart at 50 GeV - 2 TeV is identified in the 2FHL catalog, with a spectrum connecting smoothly to that measured by H.E.S.S. (Ackermann et al. 2016). On the other hand, no obvious counterparts have been found at X-ray, infrared or radio wavelengths, nor any correlations with known classes of objects such as SNRs, HII regions, star forming regions, etc.

Intriguingly, Renaud et al. (2008) discuss a potential association with the ‘‘forbidden velocity wing’’ FVW 319.8+0.3. As defined by Kang & Koo (2007), FVWs are structures observed in HI emission near the Galactic Plane at $|b| < 1.5^\circ$ with spatial extension $\lesssim 2^\circ$ and velocity deviating from Galactic rotation by more than $\sim 20 \text{ km s}^{-1}$. Of the 87 FVWs identified by Kang & Koo (2007) in large-scale HI maps with spatial and spectral resolution of 0.5° and $\sim 1 \text{ km s}^{-1}$, respectively, a few are spatially coincident with known SNRs,

HVCs, or nearby galaxies. However, no such associations were found for 85 % of their sample, and the distance and nature of most FVWs are unknown. TeVCat lists HESS J1503-582 as a “dark” source, currently the only object with such a designation.

5.2. HVC accretion origin of the dark source HESS J1503-582

As introduced in §1.2, one object in the sample of Kang & Koo (2007), FVW 40.0+0.5, was recently revealed through HI observations with higher spatial and spectral resolution (0.066° and 0.184 km s^{-1}) to consist of an expanding kpc-scale supershell with a CHVC at its geometric center (Park et al. 2016). The most natural interpretation is a HVC accretion event, that is, the impact of the CHVC at high velocity with the Galactic disk giving rise to the supershell. Park et al. (2016) favor a location in the outer Galaxy at $D \sim 20 \text{ kpc}$, which corresponds to $R \sim 15 \text{ kpc}$ at its sky position in the first Galactic quadrant. From the observed properties of the supershell and estimates of the required total energy, they infer that the CHVC began its impact $\sim 5 \times 10^6 \text{ yr}$ ago with initial kinetic energy $E_{\text{HVC}} \gtrsim 7 \times 10^{52} \text{ erg}$. Assuming a relative collision velocity $v \sim 240 \text{ km s}^{-1}$, this implies an initial mass $M_{\text{HVC}} \gtrsim 6 \times 10^4 M_\odot$, much larger than the currently observed HI mass $M_{\text{HI}} \simeq 5800 M_\odot$, which is possibly a consequence of ram pressure stripping during the accretion process.

Bolstered by this finding, we propose that HESS J1503-582, spatially coincident with FVW 319.8+0.3, also originated from a direct HVC accretion event in the outer Galaxy, and apply our model as formulated in §2 - §4. For concreteness, we focus on an interpretation based on the RS within the HVC, although a connection with the FS in the Galactic disk is not excluded. Our most uncertain parameter is the magnetic field around the shock, for which we consider a range of possible values, $B_s = 0.3 - 10 \mu\text{G}$. Otherwise, the fiducial parameter values proposed in §2 and §3 are chosen, except for some deviations in n_{HVC} , ξ_p and K_{ep} in order to provide the most consistent description of the existing observations.

For the HVC, we choose parameters similar to those inferred by Park et al. (2016) for their pre-collision CHVC: $v_s = 300 \text{ km s}^{-1}$, $M_{\text{HVC}} = 10^5 M_\odot$, and $n_{\text{HVC}} = 0.15 \text{ cm}^{-3}$, the latter implying $r_c n_{\text{HVC}} = 0.6 \text{ cm}^{-3}$ for the post-shock gas. The distance is taken to be $D = 20 \text{ kpc}$, corresponding to an impact location in the outer Galaxy at $R = 15 \text{ kpc}$ for the sky position of HESS J1503-582 in the fourth Galactic quadrant, quite analogous to the system of Park et al. (2016). These parameters give $\tau_{\text{HVC}} \simeq 1.2 \times 10^6 \text{ yr}$, $\tau_{\text{disk}} \simeq 2.0 \times 10^6 \text{ yr}$ and $\tau_{g,\text{rad}} \simeq 1.2 \times 10^6 \text{ yr}$, so that the duration of the constant velocity phase is determined by τ_{HVC} and/or $\tau_{g,\text{rad}}$. For simplicity, we assume that the event is being observed at age $t = 10^6 \text{ yr}$ after the beginning of shock formation and particle acceleration, so that quantities discussed in §3 and §4 can be evaluated with $\tau_s = t = 10^6 \text{ yr}$. At $R = 15 \text{ kpc}$, the expected ISRF (Porter et al. 2008) is approximated by two diluted black-body components with temperatures and energy densities representing the far infrared dust emission ($k_B T_{\text{dust}} = 3.0 \times 10^{-3} \text{ eV}$, $u_{\text{dust}} = 0.05 \text{ eV cm}^{-3}$) and the optical starlight ($k_B T_{\text{star}} = 0.25 \text{ eV}$, $u_{\text{star}} = 0.05 \text{ eV cm}^{-3}$), which total $u_{\text{ISRF}} = 0.1 \text{ eV cm}^{-3}$ and is subdominant compared to the CMB ($k_B T_{\text{CMB}} = 2.3 \times 10^{-4} \text{ eV}$, $u_{\text{CMB}} = 0.26 \text{ eV cm}^{-3}$). Concerning particle acceleration, we take $\eta = 1$ and $\alpha = 2$, while

tolerating large departures from $K_{ep} = 0.01$ if required by the observations (§3.3). Finally, the normalization of the proton distribution is adjusted to provide a viable fit to the gamma-ray data, and the corresponding value of ξ_p is checked a posteriori for plausibility.

Note that for a uniform spherical HVC, the above parameters give $r_{\text{HVC}} \simeq 186 \text{ pc}$ and an angular diameter $\theta \simeq 2r_{\text{HVC}}/D \simeq 1.1 \text{ deg}$, somewhat larger than the observed rms angular diameter of 0.52 deg for HESS J1503-582. However, this is not deemed to be an issue, as the gas density profile of a real CHVC is likely more centrally concentrated than a uniform distribution, not to mention the possibility of non-trivial collision geometry and projection effects, etc.

The currently available broadband data for HESS J1503-582 are shown in Figs. 3 - 6. In addition to the gamma-ray data from H.E.S.S. (Renaud et al. 2008) and Fermi-LAT (Ackermann et al. 2016), also plotted are radio and X-ray upper limits, estimated with the methods described in Abramowski et al. (2011) and originally applied to HESS J1356-645, a source with spatial extension similar to HESS J1503-582. Conservative upper limits from the Molonglo Galactic Plane Survey (MGPS) at 843 MHz and the Parkes-MIT-NRAO (PMN) survey at 4.85 GHz are 0.61 Jy and 0.62 Jy, respectively. To derive X-ray upper limits, we assume spectral index $\Gamma_X = 2$ and intervening hydrogen column density $N_{\text{H}} \simeq 1.5 \times 10^{22} \text{ cm}^{-2}$, which is the total Galactic value toward the direction of HESS J1503-582⁷ and likely comparable to the actual value at our assumed distance $D = 20 \text{ kpc}$. This gives a 3σ limit from the ROSAT All-Sky Survey (RASS) in the 1-2.4 keV band of $9 \times 10^{-12} \text{ erg cm}^{-2} \text{ s}^{-1}$.

5.3. Model results for HESS J1503-582

Compared with the broadband data of HESS J1503-582 in Figs. 3, 4, 5 and 6 are model results for $B_s = 3, 10, 1$ and $0.3 \mu\text{G}$, respectively. In order of ascending B_s , the corresponding particle maximum energies are $E_{p,\text{max}} \sim 25.6, 85, 256, 852 \text{ TeV}$ (Eq. 13) and $E_{e,\text{max}} \sim 4.7, 8.3, 11.7, 9.7 \text{ TeV}$ (Eq. 15), which can also be seen in Fig. 2. Given the limited multi-wavelength coverage of the existing data, all cases with $B_s = 0.3 - 10 \mu\text{G}$ provide generally acceptable descriptions with plausible values for ξ_p and other parameters. Nevertheless, these observations already disfavor $B_s < 0.3 \mu\text{G}$ and $B_s > 10 \mu\text{G}$, as elaborated below.

The GeV-TeV emission is dominated by the π^0 component, whose spectrum agrees fairly well with our estimates in §4.1. The inferred cutoff energies are $E_{\pi\gamma,\text{max}} \approx 0.08 E_{p,\text{max}} \sim 2.1, 6.8, 21, 68 \text{ TeV}$, ordered by B_s , within or somewhat above the energy range covered by H.E.S.S. (Fig. 2). For $B_s = 0.3 \mu\text{G}$ (Fig. 6), the model is only marginally acceptable at the highest energies, disfavoring $B_s < 0.3 \mu\text{G}$. Although the data of Renaud et al. (2008) is consistent with an unbroken power-law, the presence of spectral cutoffs can be tested with further TeV observations (§6.2).

IC and bremsstrahlung from primary electrons as well as IC from secondary e^\pm can be non-negligible in the GeV band if $B_s \lesssim 3 \mu\text{G}$. Due to Klein-Nishina effects, the primary IC spectrum is seen to peak at lower energies compared to our simple estimates in §4.2. While the contribution from primary electrons can be made more significant by choosing higher values of K_{ep} , accounting for the observed TeV emission chiefly with such components is problematic, as $E_{e,\text{max}}$ is limited to $\lesssim 12 \text{ TeV}$ (§3.2; Fig. 2).

⁷ <https://heasarc.nasa.gov/cgi-bin/Tools/w3nh/w3nh.pl>

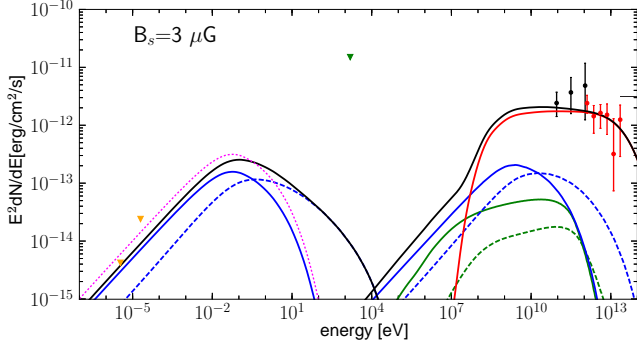


FIG. 3.— Broadband spectrum of HESS J1503-582 compared with the HVC accretion model. Observed data are from H.E.S.S. (red) and Fermi-LAT (black). Upper limits are from MGPS at 843 MHz and PMN at 4.8 GHz (yellow triangles) and RASS at 1-2.4 keV (green triangle). Model curves correspond to π^0 decay emission (red solid), synchrotron and inverse Compton emission from primary electrons (blue solid) and secondary e^\pm (blue dashed), bremsstrahlung from primary electrons (green solid) and secondary e^\pm (green dashed), and total of all components (black). Model parameters are: $v_s = 300 \text{ km s}^{-1}$, $M_{\text{HVC}} = 10^5 M_\odot$, $n_{\text{HVC}} = 0.15 \text{ cm}^{-3}$, $D = 20 \text{ kpc}$, $B_s = 3 \mu\text{G}$, $\eta = 1$, $\alpha = 2$, and $K_{ep} = 0.005$. The interstellar radiation field at $R = 15 \text{ kpc}$ is adopted. Also shown is the synchrotron emission from primary electrons only for $K_{ep} = 0.01$ (magenta dotted). The total injected proton energy is $W_p = 4.68 \times 10^{51} \text{ erg}$, corresponding to $\xi_p = 0.052$.

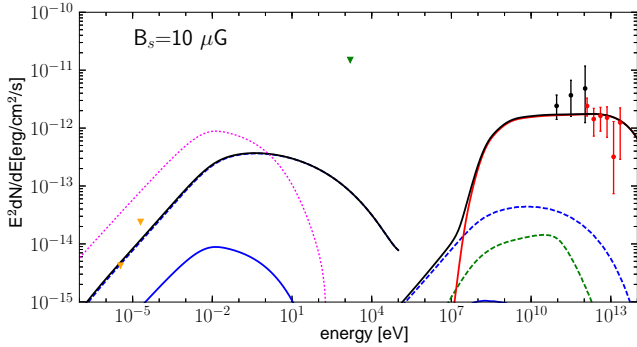


FIG. 4.— As with Fig. 3, except for $B_s = 10 \mu\text{G}$ and $K_{ep} = 10^{-4}$. The total injected proton energy is $W_p = 4.73 \times 10^{51} \text{ erg}$, corresponding to $\xi_p = 0.053$. Also shown is the synchrotron emission from primary electrons only for $K_{ep} = 0.01$ (magenta dotted).

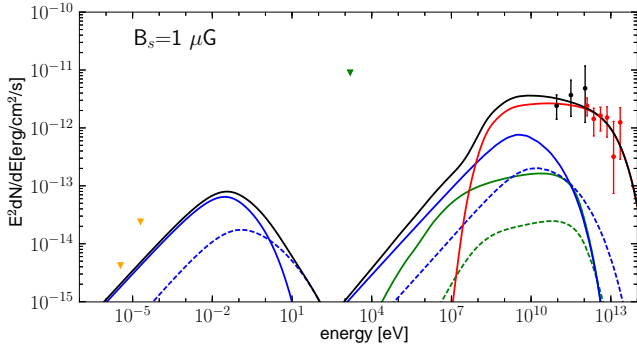


FIG. 5.— As with Fig. 3, except for $B_s = 1 \mu\text{G}$ and $K_{ep} = 0.01$. The total injected proton energy is $W_p = 5.1 \times 10^{51} \text{ erg}$, corresponding to $\xi_p = 0.057$.

When $B_s \lesssim 2 \mu\text{G}$, $E_{\text{sy,max}} \lesssim 15 \text{ eV}$, reaching only the UV band (§4.2; Eq. 22), unlike SNRs or PWNe for which the

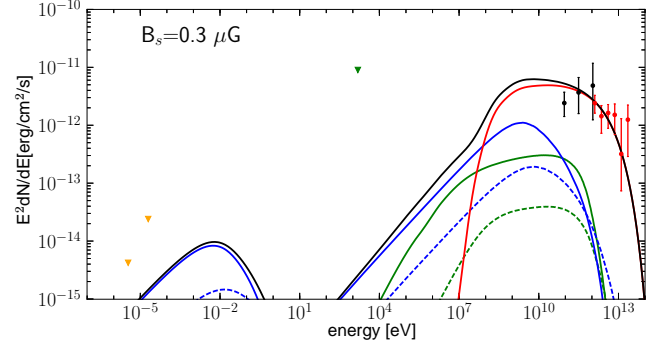


FIG. 6.— As with Fig. 3, except for $B_s = 0.3 \mu\text{G}$. The total injected proton energy is $W_p = 1.1 \times 10^{52} \text{ erg}$, corresponding to $\xi_p = 0.13$.

synchrotron emission commonly extends to X-ray energies and above. The radio emission is also faint, below the survey upper limits. Together with the expectation that the thermal emission from the shock peaks in the UV to soft X-ray bands, a range most severely affected by photoelectric absorption in the intervening ISM (Eq. 5; §6.4), this provides one plausible explanation why this source can be “dark” (i.e. not readily detectable) at wavelengths other than gamma rays.

On the other hand, when $B_s \gtrsim 3 \mu\text{G}$ (Figs. 3, 4), the synchrotron emission can be bright enough to violate the current radio upper limits, unless $K_{ep} \ll 0.01$ is invoked. We disfavor $B_s \gtrsim 10 \mu\text{G}$, since tension would persist even for the contribution from secondary e^\pm that is independent of K_{ep} (Fig. 4). The secondary synchrotron component also extends into and dominates the X-ray band for $B_s \gtrsim 3 \mu\text{G}$. While not in conflict with existing limits, this may be detectable with deeper observations by current facilities such as Chandra or XMM, which are highly desirable in order to constrain the crucial value of B_s (§6.3).

6. PROSPECTS FOR FURTHER OBSERVATIONS

We discuss further observations that can test the HVC accretion origin of dark GeV-TeV sources like HESS J1503-582 and discriminate from more conventional possibilities such as SNRs or PWNe. Also outlined are strategies to search for further sources triggered by HVC accretion events.

6.1. HI: morphology, kinematics, distance, location

As with the elucidation of FVW 40.0+0.5 as a HVC accretion event (Park et al. 2016), a pivotal test will be deeper HI observations with higher spatial and spectral resolution of the region containing FVW 319.8+0.3 and HESS J1503-582 (and other potential candidates), in order to search for morphological and kinematical evidence of a HVC, expanding shell, and/or any other sign of HVC-disk interaction. Significant improvements can be expected in the era of SKA (McClure-Griffiths et al. 2015). We note that the FVW 40.0+0.5 and FVW 319.8+0.3 systems may be at somewhat different stages of the accretion process. As discussed by Park et al. (2016), the former may be in a relatively advanced phase, well into the radiative regime, where most of the kinetic energy initially conveyed by the HVC has been radiated away, consistent with its estimated age of $5 \times 10^6 \text{ yr}$ (see Eq. 6) and the small current mass of the HVC (§5.2). In comparison, our interpretation of the latter at a younger age of $t \sim 10^6 \text{ yr}$ implies that it is only nearing the transition from adiabatic to radiative (§2.2, §3.4). Thus the conditions of the

parent HVC may be rather closer to its pre-impact state, although this can also depend on the collision parameters and geometry (Baek et al. 2008).

The kinematics information from HI observations can also provide valuable constraints on the distance. HVCs may require $M_{\text{HVC}} \gtrsim 10^{4.5} M_{\odot}$ to survive disruption in the halo before reaching the disk (§1, §2.1), and the shock requires at least $v_s \sim 120 \text{ km s}^{-1}$ to avoid suppression of particle acceleration by neutral-ion collisions (§3.4). Thus, the kinetic energy of HVCs of interest for non-thermal emission is minimally $E_{\text{HVC, min}} \sim 5 \times 10^{51} \text{ erg}$ (Eq. 7), and likely larger, as with our fiducial model parameters (§5.2). If distance constraints point to such values for the required energy, it can rule out origins related to SNRs or PWNe that are typically less energetic.

Improved constraints on the system’s sky position and distance will give better knowledge of its relative location in the Galaxy, also offering crucial clues on its origin. A unique property of HVC accretion events is that their locations with respect to Galactic star forming regions can be either weakly correlated, totally uncorrelated, or even anti-correlated, depending on the HVC’s provenance. This is in stark contrast to most other types of proposed gamma-ray emitters including SNRs and PWNe that should be closely connected with star formation. In particular, HVCs from the IGM and satellites are initially oblivious to conditions of the disk locations where they accrete, which may include regions between spiral arms as well as outside the known stellar disk. In fact, due to their typically higher angular momenta relative to the disk gas, they are more likely to accrete onto the outer regions of the Galaxy (§1.2), where the star formation rate is considerably reduced. Furthermore, SN- or SMBH-driven outflows can impede direct HVC accretion more strongly in the inner Galaxy. These effects may combine to result in a global anti-correlation. Even on smaller scales, localized outflows from individual star forming regions may have disruptive effects on HVCs falling close to them, possibly causing local anti-correlations. If some HVCs originate from Galactic fountains, their launching sites should be star forming regions, but not necessary their fallback locations, which may also be anti-correlated due to disruption by outflows from the disk.

Note that HVC-disk collisions have actually been proposed to induce star formation (e.g. Franco et al. 1988), which may be supported by some observations of the outer Galaxy (Kobayashi et al. 2008; Izumi et al. 2014). However, this is expected to occur well after the adiabatic phase of our interest, when sufficient amounts of gas has been swept up and can cool significantly. Thus the gamma-ray emitting phase of the event is unlikely to be concurrent with the phase of self-induced star formation.

6.2. GeV-TeV gamma-rays: spectra, localization, morphology

While not providing definitive proof of its origin, some expected features of the HVC accretion model can be tested by further GeV-TeV observations. The high-energy cutoff of the π^0 -dominant gamma-ray spectrum reflects $E_{p, \text{max}}$, which is determined primarily by v_s , τ_s and B_s (Eq. 13). The magnitude of v_s is controlled by the gravitational potential of the Galaxy and cannot be much larger than our fiducial value, implying the same for τ_s that depends mostly on v_s (Eqs. 3, 4, 6). Since $B_s < B_{s, \text{eq}} \sim 14 \mu\text{G}$ (§3.1), high-energy spectral cutoffs are expected somewhere in the range $\sim 2 - 100 \text{ TeV}$, as apparent in Fig. 2 and Figs. 3 - 6. Further ob-

servations by current imaging atmospheric Cherenkov telescopes (IACTs) such as H.E.S.S., MAGIC and VERITAS, ground-based arrays such as HAWC (Abeysekara et al. 2017), and future facilities such as CTA (Acharya et al. 2013) and LHAASO (Di Sciascio et al. 2016) are essential, in order to measure the cutoff and constrain key parameters such as B_s .

At lower energies, measurement of the “pion bump” around $E_{\gamma, \pi} \simeq 70 \text{ MeV}$ will verify the π^0 nature of the gamma-ray emission, an expectation in common with some SNRs (Ackermann et al. 2013) but not PWNe. The current Fermi-LAT data below a few GeV is complicated by a point source as listed in the 3FGL catalog (Acero et al. 2015) that may be separate from the 2FHL counterpart of HESS J1503-582, making difficult a robust characterization of the spectrum at these energies. Future instruments with improved localization capabilities such as e-ASTROGAM (De Angelis et al. 2017) will be advantageous.

Better knowledge of the morphology will be important at either GeV or TeV, which may be achievable by e-ASTROGAM or CTA, respectively. At most wavelengths, the spatial distribution of SNRs is generally expected to be shell-like while that of PWNe is center-filled (plerionic). HVC accretion events may be more complex, possibly being either shell-like or plerionic, both types simultaneously, or undecipherable by either type, depending on the relative importance of the FS vs RS and the collision geometry (c.f. Baek et al. 2008). Although the distinction may not be straightforward in reality as SNRs and PWNe can also have non-trivial morphology depending on their environment, improved characterization of the morphology will be undoubtedly informative.

6.3. X-ray and radio: spectra, morphology, Faraday rotation

Deeper observations in X-rays and radio continuum are warranted to search for the non-thermal synchrotron and IC emission from primary and secondary electrons, whose flux depends sensitively on our key variable B_s . Such constraints will be crucial to corroborate that B_s is sufficient to accelerate protons up to the inferred maximum energies, independently of the high-energy cutoff in the gamma-ray spectrum (§6.2).

In our models for HESS J1503-582 in §5.3, the synchrotron radio flux can exceed the sensitivity of the past MGPS and PMN surveys if $B_s \gtrsim 2 \mu\text{G}$ and $K_{ep} = 0.01$, contributed by primary electrons. The same is true if $B_s \gtrsim 10 \mu\text{G}$ irrespective of K_{ep} , due to the dominance of secondary electrons. Dedicated radio observations of this object should be worthwhile even if B_s and/or K_{ep} are lower. Although the ROSAT limits are not constraining for these models, the synchrotron X-ray flux for $B_s \gtrsim 3 \mu\text{G}$, dominated by secondary electrons and unaffected by uncertainties in K_{ep} , may be detectable with dedicated observations by current facilities such as Chandra and XMM/Newton. Note that a small fraction of the spatial extent of HESS J1503-582 that includes the X-ray source AX J150436-5824 has been observed with Chandra/ACIS-S, resulting in the detection of a faint point-like source (Anderson et al. 2014).

If such non-thermal X-ray and/or radio emission from HVC accretion events can be detected with sufficient significance, the higher angular resolution achievable in these wavebands compared to gamma-rays can be beneficial for the purpose of localization and morphological characterization, potentially allowing more detailed studies of spatial correlations, e.g. with HI properties (§6.1) and distinction from other classes of non-thermal emitters (§6.2).

Independent constraints on magnetic fields from Faraday rotation of polarized background sources will be very valuable, for both the HVC and the outer Galactic disk (§3.1). Sufficiently precise measurements may be challenging for regions in the Galactic Plane, but considerable progress is anticipated in the future with SKA (Haverkorn et al. 2015).

6.4. Other wavelengths: thermal signatures

Assuming for simplicity the shocked volume V_s to be a spherical region of radius r_s , the post-shock gas heated to $T_s \simeq 1.3 \times 10^6$ K $\simeq 0.11$ keV (Eq. 5) will give rise to thermal bremsstrahlung (free-free) emission at photon energy $\epsilon > k_B T_s$ with energy flux

$$\begin{aligned} \epsilon f_{\text{ff}}(\epsilon) &= \frac{32\sqrt{2}\pi e^6}{3hm_e^{3/2}c^3} \epsilon^{1/2} \exp\left(-\frac{\epsilon}{k_B T_s}\right) (r_c n_0)^2 \frac{V_s}{4\pi D^2} \\ &\simeq 4.9 \times 10^{-9} \text{ erg cm}^{-2} \text{ s}^{-1} \left(\frac{\epsilon}{0.1 \text{ keV}}\right)^{1/2} \exp\left(-\frac{\epsilon}{k_B T_s}\right) \\ &\quad \times \left(\frac{r_c n_0}{0.4 \text{ cm}^{-3}}\right)^2 \left(\frac{r_s}{200 \text{ pc}}\right)^3 \left(\frac{D}{20 \text{ kpc}}\right)^{-2} \quad (25) \end{aligned}$$

where e is the elementary charge, the Gaunt factor $g_{ff} = (3k_B T_s / \pi \epsilon)^{1/2}$ is adopted as appropriate for $T_s > 13.6$ eV and $\epsilon > k_B T_s$, and only the contribution from fully ionized hydrogen is considered (Rybicki & Lightman 1979; Draine 2011).

Emission in the UV to soft X-ray bands is attenuated during propagation in the ISM by a factor $\exp[-\tau_{\text{pe}}(\epsilon)]$, where $\tau_{\text{pe}}(\epsilon) = \sigma_{\text{pe}}(\epsilon) N_{\text{H}}$ is the optical depth to the source, and $\sigma_{\text{pe}}(\epsilon)$ is the effective cross section for photoelectric absorption by all elements in the ISM, which increases steeply with decreasing ϵ down to 13.6 eV (e.g. Kaastra et al. 2008). Thus the observable spectrum peaks in a certain range of ϵ , being exponentially suppressed both above and below. Taking $N_{\text{H}} \simeq 1.5 \times 10^{22} \text{ cm}^{-2}$ as appropriate for HESS J1503-582 at our assumed distance $D = 20$ kpc (§5.2), $\tau_{\text{pe}} \simeq 10, 3.2$ and 0.63 at $\epsilon \sim 0.5, 1$ and 2 keV, respectively. Combined with Eq. 25, we estimate $\epsilon f_{\text{ff}}(\epsilon) \exp[-\tau_{\text{pe}}(\epsilon)] \gtrsim 10^{-15} \text{ erg cm}^{-2} \text{ s}^{-1}$ for $0.5 < \epsilon < 1.7$ keV, peaking at $\sim 8.1 \times 10^{-14} \text{ erg cm}^{-2} \text{ s}^{-1}$ for $\epsilon \sim 0.9$ keV. Note that these values are sensitive to even small changes in T_s or N_{H} . Considering the very narrow spectrum, spatial extension of $\sim 0.5^\circ$ and source confusion effects in the Galactic Plane, detecting this with current facilities such as Chandra or XMM/Newton could be difficult. Nevertheless, if similar sources are found in the future at distances or locations with much less N_{H} , for example, in suitable regions in the second or third Galactic quadrants, detection of the thermal continuum might still be feasible and provide strong support for a HVC accretion event.

Although a detailed discussion is beyond the scope of this paper, various other types of thermal signatures including emission lines also provide valuable diagnostics. Compared to many other known classes of interstellar shock phenomena, such features are generally expected to be weaker here due to the lower density and lower metallicity of both the HVC and the outer Galactic disk, especially those related to molecules or dust. On the other hand, with $Z/Z_\odot \sim 0.2$ and $T_s \sim 10^6$ K, metals such as Fe still play a dominant role as gas coolants (Draine 2011), and the likelihood that our shocks are moderately radiative (§2.2, §3.4) entails some level of associated line emission, in addition to certain transitions of hydrogen and helium. Subject to interstellar attenuation as described

above, their detection may be challenging but would be extremely valuable, potentially allowing direct confirmation of the shock velocities characteristic of HVCs, not to mention further important constraints on the source distance.

6.5. High-energy neutrinos

Detection of high-energy neutrinos from the source would offer unequivocal proof that protons are accelerated therein to energies approaching PeV, if not more detailed information regarding its origin. With our HVC accretion model parameters for HESS J1503-582, neutrinos are produced via pp collisions up to maximum energies $E_{\nu, \text{max}} \approx 0.04 E_{p, \text{max}} \sim 1\text{--}34$ TeV for $B_s = 0.3\text{--}10 \mu\text{G}$ (Fig. 2; §6.2). For $B_s > 3 \mu\text{G}$ and $D = 20$ kpc, the estimated neutrino flux per flavor at $E_\nu \sim 10$ TeV is $E_\nu^2 dN_{\nu, pp}/dE_\nu \simeq 1.8 \times 10^{-12} \text{ erg cm}^{-2} \text{ s}^{-1}$ (Eq. 20). At $E_\nu \lesssim 40$ TeV, the angular resolution of IceCube for through-going track events is $\gtrsim 0.5^\circ$, so sources similar to HESS J1503-582 can be considered point-like. Compared with the 5σ discovery potential of IceCube for point sources of muon neutrinos at $E_\nu \gtrsim 10$ TeV (Aartsen et al. 2017), the predicted flux is about an order of magnitude below for a northern source at declination $\delta > 0^\circ$, and up to 2-3 orders of magnitude below for a southern source such as HESS J1503-582. Nevertheless, if similar sources can be found in the northern hemisphere in the future, they could still be interesting for IceCube, especially if its sensitivity at lower energies can be enhanced (Aartsen et al. 2016). Better yet, realistic prospects of detecting neutrinos from southern Galactic sources including HESS J1503-582 may become feasible with KM3NeT (Adrián-Martínez et al. 2016).

6.6. Searches for HVC accretion events

As discussed in §2.3, the expected total number of active HVC accretion events in the Galaxy with shocks in the adiabatic phase producing multi-TeV emission is fiducially $N_s \sim 10$, but can be larger or smaller depending on the unknown distribution of v_{acc} and M_{HVC} . If such shocks continue to accelerate particles into their radiative phase, a larger number of sources with sub-TeV emission may result, perhaps with a spectral break, as discussed in some models for old SNRs (§3.4). Searches are warranted for further candidate HVC accretion events in all wavebands and channels discussed above, but particularly at GeV-TeV energies and in HI.

Unidentified sources in the Galactic Plane found by H.E.S.S. and other IACTs, HAWC, and Fermi should be scrutinized for correlations with prominent HI structures such as FVWs, which will be facilitated in the future by CTA and e-ASTROGAM with their higher angular resolution. Similar studies for high-energy neutrinos detected near the Galactic Plane may also be interesting. Alternatively, one can select particularly interesting FVWs or other objects with noteworthy HI properties and perform targeted IACT observations, keeping in mind the expectations noted in §6.1 such as likely location in the outer Galaxy with little, no or opposite correlation with star forming regions. We note that while the CHVC+supershell system of Park et al. (2016) may be deep into its radiative phase and possibly less efficient as a particle accelerator (§6.1), dedicated observations of the region may still be worthwhile. The available HI data should improve dramatically with the advent of SKA (McClure-Griffiths et al. 2015).

A very intriguing possibility is the detection of HVC accretion events in external galaxies such as M31. HVCs have

been observed within projected distance ~ 100 kpc of M31 with estimated HI masses $M_{\text{HI}} \sim 10^5 - 10^7 M_{\odot}$ (Thilker et al. 2004; Westmeier et al. 2008; Lockman 2017). If a relatively large HVC of total mass $M_{\text{HVC}} \sim 5 \times 10^6 M_{\odot}$ is accreting at $v_{\text{acc}} \sim 300$ km s $^{-1}$ onto the the disk of M31 at distance $D = 780$ kpc, protons shock-accelerated therein to $E_p \sim 50$ TeV can give rise to pp π^0 gamma-rays at $E_{\gamma} \sim 4$ TeV with energy flux $E_{\gamma}^2 dN_{\gamma,pp}/dE_{\gamma} \simeq 1.1 \times 10^{-13}$ erg cm $^{-2}$ s $^{-1}$, taking the same parameters as in Eq. 19 except for E_p , $L_{k,\text{HVC}}$ and D . This may be within reach of the sensitivity of CTA North ⁸, potentially offering unique information on HVC accretion in a disk galaxy other than our own, even though the likelihood of such an energetic accretion event occurring at a given time may not be large (~ 20 % from Eq.11 if $\dot{M}_{\text{acc,HVC}}$ for M31 is similar to the Milky Way).

7. CONCLUSIONS AND PROSPECTS

As observationally established facts:

1. The Galactic disk is accreting low-metallicity gas at a total rate of order $\sim 1M_{\odot}\text{yr}^{-1}$.
2. At least part of this accretion proceeds in the form of high velocity clouds of cool gas with mass $\sim 10^5 M_{\odot}$ and mean gas density ~ 0.1 cm $^{-3}$ directly impacting the outer regions of the disk at velocities of a few 100 km s $^{-1}$, as seen in an object initially identified as a forbidden velocity wing.
3. Numerous GeV-TeV sources in the Galactic Plane are spatially extended and unidentified, one of which (HESS J1503-582) is dark (undetected in any other waveband) except for spatial association with a forbidden velocity wing of unknown physical nature.

Facts 1 and 2 entails the formation of collisionless adiabatic shocks with lifetime $\sim 10^6$ yr. Assuming shock velocity $v_s \sim 300$ km s $^{-1}$ and magnetic fields of order a few μG , protons and electrons can be accelerated up to sub-PeV and multi-TeV energies, respectively, resulting in GeV-TeV gamma-ray emission primarily via p-p π^0 decay with some additional contribution from inverse Compton. Part of Fact 3 concerning HESS J1503-582 can be consistently and plausibly accounted for in such terms. Despite the currently limited multi-wavelength data, the observed TeV spectrum and upper limits on radio synchrotron emission from secondary e^{\pm} imply the constraint $B_s \sim 0.3 - 10$ μG .

Further observational tests of HVC accretion events as gamma-ray emitters include better HI observations of promising GeV-TeV sources to clarify their morphology and kinematics and to constrain their distance and locations that may be weakly correlated, not correlated at all, or even anti-correlated with star-forming regions, deeper X-ray and radio observations of such sources to detect synchrotron components and constrain B_s , as well as dedicated TeV observations of objects selected in HI such as FVWs. Searches are worthwhile for more such sources in surveys of the Galactic Plane at GeV-TeV and in HI, and possibly even external galaxies like M31.

Our theoretical formulation can be improved in various respects. For shock properties, the lack of symmetry in the problem calls for 3-D hydrodynamical simulations including radiative cooling effects for a better description of its dynamical evolution and dependence on collision parameters (§2.2).

The plasma physics of particle acceleration at low shock velocities of our interest is worth exploring in detail through particle-in-cell simulations, including the potential effects of magnetic field amplification (§3.1) and charge exchange reactions induced by neutral particles (§3.4).

We have focused on non-thermal emission induced by CRs at the source, and have not explicitly addressed the consequences of CRs escaping from them. While the contribution of HVC accretion to the total Galactic CR budget is estimated to be minor, ~ 5 % or less (§2.3), it can still be relatively important in the outer disk regions, where the occurrence of conventional CR sources like SNRs are much rarer (§1.2, §6.1). For example, compared to $R \sim 4$ kpc where Galactic star formation peaks, the star formation rate as traced by SNRs or pulsars is $\gtrsim 10$ times lower at $R \gtrsim 15$ kpc (Stahler & Palla 2005). Considering the likelihood that the radial dependence of gas accretion is biased outwards relative to star formation in the disk (Peek 2009; Christensen et al. 2016; Stewart 2017), CRs of HVC accretion origin may even be dominant in the outer Galaxy. This can have interesting implications for the diffuse Galactic gamma-ray emission, whose observed intensity at $R > R_{\odot}$ has long known to be in excess of expectations based on CR sources that track star formation (Ackermann et al. 2012; Acero et al. 2016). The observed contrast between spiral arm and inter-arm regions also appears to be in tension with CRs tracing star formation (Grenier et al. 2015). Proposed solutions to the discrepancy include non-conventional modes of CR diffusion (e.g. Evoli et al. 2012), and dark gas missed by existing observations (Grenier et al. 2015). The intriguing prospect that CRs induced by HVC accretion is behind this mystery will be discussed in a future publication.

Finally, we touch on the possibility that future observations of non-thermal phenomena triggered by accretion of cool gas may provide a fresh perspective on studying gas accretion processes onto galaxies per se, many aspects of which are still poorly understood (Fox & Davé 2017). As discussed above, HVC accretion events are objects that may not be readily detectable at wavelengths other than GeV-TeV gamma rays, with heavily attenuated thermal emission (§6.4), possibly accompanied by weak and diffuse radio and X-ray emission (§5.3, §6.3). Their clear identification may only be feasible by HI observations with high angular and spectral resolution (§6.1). While GeV-TeV emission does not provide unique indication of HVC accretion nor detailed information on properties of the parent HVC, they do potentially serve as signposts that illuminate the accretion interface and are visible across the Galaxy to its outer edges, and perhaps also in the nearest external galaxies such as M31 (§6.6). If at least some GeV-TeV sources can be revealed to be HVC accretion events via follow-up observations in HI and other wavelengths, the same observations should constrain their distance and location, and thereby provide information on key parameters of the HVC such as its mass, velocity, density and temperature. Achieving a sufficient sample of such observations at different locations in the Galaxy could allow characterization of the distribution of these parameters and its spatial dependence, which is highly uncertain at present (§2.1). This in turn could offer potential discrimination of the source(s) of the accreting gas, among IGM filaments, satellite galaxies, halo condensation, etc. In addition, non-thermal emission offers direct constraints on magnetic fields, which may not be easily obtainable otherwise. As accretion of cold gas is likely more efficient at early epochs (§1.1), related processes that may

⁸ <https://www.cta-observatory.org>

have occurred in the past and left observable traces, e.g. CR-induced production of light elements (Suzuki & Inoue 2002), are also worth exploring. Such studies can offer a novel approach to probe gas accretion processes and the evolutionary cycle of baryons in the Milky Way and other galaxies.

We acknowledge valuable discussions with Changhyun

Baek, Takahiro Kudoh, Yutaka Ohira, Ryo Yamazaki, Masahiro Nagashima and Masaki Mori. This work is supported by JSPS KAKENHI Grant Numbers JP17K05460 (SI) and JP26247027 (YU), and by the RIKEN Junior Research Associate Program (MA).

REFERENCES

- Aartsen, M. G., Abraham, K., Ackermann, M., et al. 2016, *ArXiv e-prints* —, 2017, *ApJ*, 835, 151
- Abdalla, H., Abramowski, A., Aharonian, F., et al. 2017, *ArXiv e-prints*
- Abdo, A. A., Allen, B., Berley, D., et al. 2007, *ApJ*, 664, L91
- Abeysekara, A. U., Albert, A., Alfaro, R., et al. 2017, *ApJ*, 843, 40
- Abramowski, A., Acero, F., Aharonian, F., et al. 2011, *A&A*, 533, A103
- Acero, F., Ackermann, M., Ajello, M., et al. 2015, *ApJS*, 218, 23
- , 2016, *ApJS*, 223, 26
- Acharya, B. S., Actis, M., Aghajani, T., et al. 2013, *Astroparticle Physics*, 43, 3
- Ackermann, M., Ajello, M., Allafort, A., et al. 2013, *Science*, 339, 807
- Ackermann, M., Ajello, M., Atwood, W. B., et al. 2012, *ApJ*, 750, 3
- , 2016, *ApJS*, 222, 5
- Ackermann, M., Ajello, M., Baldini, L., et al. 2017, *ApJ*, 843, 139
- Adam, R., Ade, P. A. R., Alves, M. I. R., et al. 2016, *A&A*, 596, A103
- Adrián-Martínez, S., Ageron, M., Aharonian, F., et al. 2016, *Journal of Physics G Nuclear Physics*, 43, 084001
- Aharonian, F., Akhperjanian, A., Beilicke, M., et al. 2002, *A&A*, 393, L37
- Aharonian, F., Akhperjanian, A. G., Aye, K.-M., et al. 2005, *Science*, 307, 1938
- Aharonian, F., Akhperjanian, A. G., Barres de Almeida, U., et al. 2008, *A&A*, 477, 353
- Aharonian, F., Akhperjanian, A. G., Bazer-Bachi, A. R., et al. 2006, *ApJ*, 636, 777
- Aharonian, F. A. 2004, *Very high energy cosmic gamma radiation : a crucial window on the extreme Universe* (World Scientific Publishing Co)
- Aleksić, J., Ansoldi, S., Antonelli, L. A., et al. 2014, *A&A*, 571, A96
- Anderson, G. E., Gaensler, B. M., Kaplan, D. L., et al. 2014, *ApJS*, 212, 13
- Armiglotta, L., Fraternali, F., Werk, J. K., Prochaska, J. X., & Marinacci, F. 2017, *MNRAS*, 470, 114
- Atoyan, A., Buckley, J., & Krawczynski, H. 2006, *ApJ*, 642, L153
- Baek, C. H., Kudoh, T., & Tomisaka, K. 2008, *ApJ*, 682, 434
- Bartoli, B., Bernardini, P., Bi, X. J., et al. 2013, *ApJ*, 779, 27
- Beck, M. C., Beck, A. M., Beck, R., Dolag, K., Strong, A. W., & Nielaba, P. 2016, *JCAP*, 5, 056
- Beck, R. 2016, *A&A Rev.*, 24, 4
- Bell, A. R. 1978, *MNRAS*, 182, 147
- , 2004, *MNRAS*, 353, 550
- Binney, J. 1977, *ApJ*, 215, 483
- Birnboim, Y. & Dekel, A. 2003, *MNRAS*, 345, 349
- Bland-Hawthorn, J. & Gerhard, O. 2016, *ARA&A*, 54, 529
- Blandford, R. & Eichler, D. 1987, *Phys. Rep.*, 154, 1
- Blandford, R. D. & Ostriker, J. P. 1978, *ApJ*, 221, L29
- Blasi, P. 2013, *A&A Rev.*, 21, 70
- Brooks, A. M., Governato, F., Quinn, T., Brook, C. B., & Wadsley, J. 2009, *ApJ*, 694, 396
- Bykov, A. M., Chevalier, R. A., Ellison, D. C., & Uvarov, Y. A. 2000, *ApJ*, 538, 203
- Caprioli, D. 2015, in *International Cosmic Ray Conference*, Vol. 34, 34th International Cosmic Ray Conference (ICRC2015), ed. A. S. Borisov, V. G. Denisova, Z. M. Guseva, et al., 8
- Christensen, C. R., Davé, R., Governato, F., Pontzen, A., Brooks, A., Munshi, F., Quinn, T., & Wadsley, J. 2016, *ApJ*, 824, 57
- Combes, F. 2014, in *Astronomical Society of the Pacific Conference Series*, Vol. 480, *Structure and Dynamics of Disk Galaxies*, ed. M. S. Seigar & P. T. P. Truethardt, 211
- De Angelis, A., Tatischeff, V., Tavani, M., et al. 2017, *Experimental Astronomy*
- de Jager, O. C., Ferreira, S. E. S., Djannati-Ataï, A., Dalton, M., Deil, C., Kosack, K., Renaud, M., Schwanke, U., & Tibolla, O. 2009, *ArXiv e-prints*
- Deil, C., Brun, F., Carrigan, S., et al. 2015, in *International Cosmic Ray Conference*, Vol. 34, 34th International Cosmic Ray Conference (ICRC2015), ed. A. S. Borisov, V. G. Denisova, Z. M. Guseva, et al., 773
- Dermer, C. D. & Menon, G. 2009, *High Energy Radiation from Black Holes: Gamma Rays, Cosmic Rays, and Neutrinos* (Princeton University Press)
- Di Sciacio, G. et al. 2016, *ArXiv e-prints*
- Donath, A., Brun, F., Chaves, R. C. G., Deil, C., Marandon, V., Terrier, R., & H.E.S.S. Collaboration. 2017, in *American Institute of Physics Conference Series*, Vol. 1792, 6th International Symposium on High Energy Gamma-Ray Astronomy, 040001
- D’Onghia, E. & Fox, A. J. 2016, *ARA&A*, 54, 363
- Draine, B. T. 2011, *Physics of the Interstellar and Intergalactic Medium* (Princeton University Press)
- Drury, L. O., Aharonian, F. A., & Voelk, H. J. 1994, *A&A*, 287, 959
- Drury, L. O., Duffy, P., & Kirk, J. G. 1996, *A&A*, 309, 1002
- Evoli, C., Gaggero, D., Grasso, D., & Maccione, L. 2012, *Physical Review Letters*, 108, 211102
- Faucher-Giguère, C.-A., Kereš, D., & Ma, C.-P. 2011, *MNRAS*, 417, 2982
- Fernández, X., Joung, M. R., & Putman, M. E. 2012, *ApJ*, 749, 181
- Ferrière, K. M. 2001, *Reviews of Modern Physics*, 73, 1031
- Finlator, K. 2017, in *Astrophysics and Space Science Library*, Vol. 430, *Astrophysics and Space Science Library*, ed. A. Fox & R. Davé, 221
- Fox, A. & Davé, R., eds. 2017, *Astrophysics and Space Science Library*, Vol. 430, *Gas Accretion onto Galaxies*
- Fox, A. J., Lehner, N., Lockman, F. J., et al. 2016, *ApJ*, 816, L11
- Fox, A. J., Wakker, B. P., Barger, K. A., et al. 2014, *ApJ*, 787, 147
- Franco, J., Tenorio-Tagle, G., Bodenheimer, P., Rozyczka, M., & Mirabel, I. F. 1988, *ApJ*, 333, 826
- Fraternali, F. 2017, in *Astrophysics and Space Science Library*, Vol. 430, *Astrophysics and Space Science Library*, ed. A. Fox & R. Davé, 323
- Galyardt, J. & Shelton, R. L. 2016, *ApJ*, 816, L18
- Ginzburg, V. L. & Syrovatskii, S. I. 1964, *The Origin of Cosmic Rays* (New York: Macmillan)
- Gottschall, D., Capasso, M., Deil, C., et al. 2016, *ArXiv e-prints*
- Grenier, I. A., Black, J. H., & Strong, A. W. 2015, *ARA&A*, 53, 199
- Guo, X., Sironi, L., & Narayan, R. 2014, *ApJ*, 794, 153
- Haverkorn, M. 2015, in *Astrophysics and Space Science Library*, Vol. 407, *Magnetic Fields in Diffuse Media*, ed. A. Lazarian, E. M. de Gouveia Dal Pino, & C. Melioli, 483
- Haverkorn, M., Akahori, T., Carretti, E., et al. 2015, *Advancing Astrophysics with the Square Kilometre Array (AASKA14)*, 96
- Heiles, C. 1984, *ApJS*, 55, 585
- Heitsch, F. & Putman, M. E. 2009, *ApJ*, 698, 1485
- Henry, R. B. C. & Worthey, G. 1999, *PASP*, 111, 919
- Hill, A. S., Mao, S. A., Benjamin, R. A., Lockman, F. J., & McClure-Griffiths, N. M. 2013, *ApJ*, 777, 55
- Hollenbach, D. & McKee, C. F. 1989, *ApJ*, 342, 306
- Inoue, Y., Lee, S.-H., Tanaka, Y. T., & Kobayashi, S. B. 2017, *Astroparticle Physics*, 90, 14
- Ioka, K. & Mészáros, P. 2010, *ApJ*, 709, 1337
- Izumi, N., Kobayashi, N., Yasui, C., Tokunaga, A. T., Saito, M., & Hamano, S. 2014, *ApJ*, 795, 66
- Jansson, R. & Farrar, G. R. 2012, *ApJ*, 761, L11
- Joung, M. R., Bryan, G. L., & Putman, M. E. 2012a, *ApJ*, 745, 148
- Joung, M. R., Putman, M. E., Bryan, G. L., Fernández, X., & Peek, J. E. G. 2012b, *ApJ*, 759, 137
- Kaastra, J. S., Paerels, F. B. S., Durret, F., Schindler, S., & Richter, P. 2008, *Space Sci. Rev.*, 134, 155
- Kachelriess, M., Moskalenko, I. V., & Ostapchenko, S. S. 2014, *ApJ*, 789, 136
- Kalberla, P. M. W. & Kerp, J. 2009, *ARA&A*, 47, 27
- Kang, H. & Ryu, D. 2013, *ApJ*, 764, 95
- Kang, J.-h. & Koo, B.-C. 2007, *ApJS*, 173, 85
- Kereš, D., Katz, N., Weinberg, D. H., & Davé, R. 2005, *MNRAS*, 363, 2
- Kobayashi, N., Yasui, C., Tokunaga, A. T., & Saito, M. 2008, *ApJ*, 683, 178
- Kudoh, T. & Basu, S. 2004, *A&A*, 423, 183
- Kwak, K., Henley, D. B., & Shelton, R. L. 2011, *ApJ*, 739, 30
- Larson, R. B. 1972, *Nature*, 236, 21
- Lee, S.-H., Patnaude, D. J., Raymond, J. C., Nagataki, S., Slane, P. O., & Ellison, D. C. 2015, *ApJ*, 806, 71
- Lehner, N. & Howk, J. C. 2011, *Science*, 334, 955
- Lockman, F. J. 2017, in *Astrophysics and Space Science Library*, Vol. 430, *Astrophysics and Space Science Library*, ed. A. Fox & R. Davé, 49
- Malkov, M. A., Diamond, P. H., & Sagdeev, R. Z. 2011, *Nature Communications*, 2, 194
- Malkov, M. A. & Drury, L. O. 2001, *Reports on Progress in Physics*, 64, 429
- Marinacci, F., Binney, J., Fraternali, F., Nipoti, C., Ciotti, L., & Londrillo, P. 2010, *MNRAS*, 404, 1464
- Matteucci, F. 2014, *The Origin of the Galaxy and Local Group, Saas-Fee Advanced Course*, Volume 37. ISBN 978-3-642-41719-1. Springer-Verlag Berlin Heidelberg, 2014, p. 145, 37, 145
- McClure-Griffiths, N. M., Madsen, G. J., Gaensler, B. M., McConnell, D., & Schnitzler, D. H. F. M. 2010, *ApJ*, 725, 275

- McClure-Griffiths, N. M., Stanimirovic, S., Murray, C., et al. 2015, *Advancing Astrophysics with the Square Kilometre Array (AASKA14)*, 130
- McClure-Griffiths, N. M., Staveley-Smith, L., Lockman, F. J., Calabretta, M. R., Ford, H. A., Kalberla, P. M. W., Murphy, T., Nakanishi, H., & Pisano, D. J. 2008, *ApJ*, 673, L143
- McCourt, M., O'Leary, R. M., Madigan, A.-M., & Quataert, E. 2015, *MNRAS*, 449, 2
- Mori, M. 2009, *Astroparticle Physics*, 31, 341
- Morlino, G., Blasi, P., Bandiera, R., Amato, E., & Caprioli, D. 2013, *ApJ*, 768, 148
- Murante, G., Calabrese, M., De Lucia, G., Monaco, P., Borgani, S., & Dolag, K. 2012, *ApJ*, 749, L34
- Murase, K., Inoue, S., & Nagataki, S. 2008, *ApJ*, 689, L105
- Nelson, D., Vogelsberger, M., Genel, S., Sijacki, D., Kereš, D., Springel, V., & Hernquist, L. 2013, *MNRAS*, 429, 3353
- Nichols, M. & Bland-Hawthorn, J. 2009, *ApJ*, 707, 1642
- Nuza, S. E., Parisi, F., Scannapieco, C., Richter, P., Gottlöber, S., & Steinmetz, M. 2014, *MNRAS*, 441, 2593
- Ohira, Y. 2012, *ApJ*, 758, 97
- Oort, J. H. 1970, *A&A*, 7, 381
- Park, G., Koo, B.-C., Kang, J.-h., Gibson, S. J., Peek, J. E. G., Douglas, K. A., Korpela, E. J., & Heiles, C. E. 2016, *ApJ*, 827, L27
- Peek, J. E. G. 2009, *ApJ*, 698, 1429
- Porter, T. A., Moskalenko, I. V., Strong, A. W., Orlando, E., & Bouchet, L. 2008, *ApJ*, 682, 400
- Putman, M. E. 2017, in *Astrophysics and Space Science Library*, Vol. 430, *Astrophysics and Space Science Library*, ed. A. Fox & R. Davé, 1
- Putman, M. E., Peek, J. E. G., & Joung, M. R. 2012, *ARA&A*, 50, 491
- Rees, M. J. & Ostriker, J. P. 1977, *MNRAS*, 179, 541
- Renaud, M., Goret, P., & Chaves, R. C. G. 2008, in *American Institute of Physics Conference Series*, Vol. 1085, *American Institute of Physics Conference Series*, ed. F. A. Aharonian, W. Hofmann, & F. Rieger, 281–284
- Richter, P. 2012, *ApJ*, 750, 165
- Richter, P. 2017, in *Astrophysics and Space Science Library*, Vol. 430, *Astrophysics and Space Science Library*, ed. A. Fox & R. Davé, 15
- Rybicki, G. B. & Lightman, A. P. 1979, *Radiative processes in astrophysics* (Wiley-Interscience)
- Sánchez Almeida, J., Elmegreen, B. G., Muñoz-Tuñón, C., & Elmegreen, D. M. 2014, *A&A Rev.*, 22, 71
- Sancisi, R., Fraternali, F., Oosterloo, T., & van der Hulst, T. 2008, *A&A Rev.*, 15, 189
- Shapiro, P. R. & Field, G. B. 1976, *ApJ*, 205, 762
- Shull, J. M. & McKee, C. F. 1979, *ApJ*, 227, 131
- Silk, J. 1977, *ApJ*, 211, 638
- Spitzer, Jr., L. 1956, *ApJ*, 124, 20
- Stahler, S. W. & Palla, F. 2005, *The Formation of Stars* (Wiley-VCH), 865
- Stewart, K. R. 2017, in *Astrophysics and Space Science Library*, Vol. 430, *Astrophysics and Space Science Library*, ed. A. Fox & R. Davé, 249
- Stewart, K. R., Kaufmann, T., Bullock, J. S., Barton, E. J., Maller, A. H., Diemand, J., & Wadsley, J. 2011, *ApJ*, 738, 39
- Strong, A. W., Porter, T. A., Digel, S. W., Jóhannesson, G., Martin, P., Moskalenko, I. V., Murphy, E. J., & Orlando, E. 2010, *ApJ*, 722, L58
- Suzuki, T. K. & Inoue, S. 2002, *ApJ*, 573, 168
- Tenorio-Tagle, G. 1980, *A&A*, 88, 61
- . 1981, *A&A*, 94, 338
- Tenorio-Tagle, G. & Bodenheimer, P. 1988, *ARA&A*, 26, 145
- Tenorio-Tagle, G., Bodenheimer, P., Rozyczka, M., & Franco, J. 1986, *A&A*, 170, 107
- Tenorio-Tagle, G., Franco, J., Bodenheimer, P., & Rozyczka, M. 1987, *A&A*, 179, 219
- Thilker, D. A., Braun, R., Walterbos, R. A. M., Corbelli, E., Lockman, F. J., Murphy, E., & Maddalena, R. 2004, *ApJ*, 601, L39
- Tibaldo, L., Digel, S. W., Casandjian, J. M., et al. 2015, *ApJ*, 807, 161
- Uchiyama, Y., Aharonian, F. A., Tanaka, T., Takahashi, T., & Maeda, Y. 2007, *Nature*, 449, 576
- Uchiyama, Y., Blandford, R. D., Funk, S., Tajima, H., & Tanaka, T. 2010, *ApJ*, 723, L122
- van de Voort, F. 2017, in *Astrophysics and Space Science Library*, Vol. 430, *Astrophysics and Space Science Library*, ed. A. Fox & R. Davé, 301
- van de Voort, F., Schaye, J., Booth, C. M., Haas, M. R., & Dalla Vecchia, C. 2011, *MNRAS*, 414, 2458
- Wakely, S. P. & Horan, D. 2008, *International Cosmic Ray Conference*, 3, 1341
- Wakker, B. P. & van Woerden, H. 1997, *ARA&A*, 35, 217
- Weinstein, A. et al. 2009, *ArXiv e-prints*
- Westmeier, T., Brüns, C., & Kerp, J. 2008, *MNRAS*, 390, 1691
- White, S. D. M. & Frenk, C. S. 1991, *ApJ*, 379, 52
- White, S. D. M. & Rees, M. J. 1978, *MNRAS*, 183, 341
- Yamazaki, R., Kohri, K., Bamba, A., Yoshida, T., Tsuribe, T., & Takahara, F. 2006, *MNRAS*, 371, 1975
- Yao, J. M., Manchester, R. N., & Wang, N. 2017, *ApJ*, 835, 29